

Finding universal structures in quantum many-body dynamics via persistent homology

D. Spitz^{1*}, J. Berges¹, M. Oberthaler², A. Wienhard^{3, 4}

¹ Institut für theoretische Physik, Ruprecht-Karls-Universität Heidelberg,
Philosophenweg 16, 69120 Heidelberg, Germany

² Kirchhoff-Institut für Physik, Ruprecht-Karls-Universität Heidelberg, Im Neuenheimer
Feld 227, 69120 Heidelberg, Germany

³ Mathematisches Institut, Ruprecht-Karls-Universität Heidelberg, Im Neuenheimer Feld
205, 69120 Heidelberg, Germany

⁴ HITS gGmbH, Heidelberg Institute for Theoretical Studies, Schloss-Wolfsbrunnenweg
35, 69118 Heidelberg, Germany

* spitz@thphys.uni-heidelberg.de

January 29, 2021

1 Abstract

² Inspired by topological data analysis techniques, we introduce persistent ho-
³ mology observables and apply them in a geometric analysis of the dynamics
⁴ of quantum field theories. As a prototype application, we consider data from
⁵ a classical-statistical simulation of a two-dimensional Bose gas far from equi-
⁶ librium. We discover a continuous spectrum of dynamical scaling exponents,
⁷ which provides a refined classification of nonequilibrium universal phenom-
⁸ ena. A possible explanation of the underlying processes is provided in terms
⁹ of mixing strong wave turbulence and anomalous vortex kinetics components
¹⁰ in point clouds. We find that the persistent homology scaling exponents are
¹¹ inherently linked to the geometry of the system, as the derivation of a packing
¹² relation reveals. The approach opens new ways of analyzing quantum many-
¹³ body dynamics in terms of robust topological structures beyond standard field
¹⁴ theoretic techniques.

¹⁵

16 Contents

¹⁷	1 Introduction	2
¹⁸	2 Persistent homology in a Bose gas	4
¹⁹	2.1 Simulation prerequisites	4
²⁰	2.2 Phenomenology of point clouds	6
²¹	2.3 An introduction to persistent homology	7
²²	2.3.1 Alpha complexes	7
²³	2.3.2 Persistent homology and the persistence diagram	9
²⁴	2.3.3 Statistical measures: birth and death radii distributions	10
²⁵	2.4 Growing geometric structures in persistent homology	11
²⁶	2.5 Unveiling a spectrum of scaling exponents	12
²⁷	2.6 Scaling species and exponents mixing conjecture	13
²⁸	3 Persistent homology observables and self-similarity	14

29	3.1	Persistent homology observables via functional summaries	15
30	3.2	The asymptotic persistence pair distribution and geometric quantities	15
31	3.3	Self-similar scaling approach	17
32	3.3.1	Scaling ansatz to the asymptotic persistence pair distribution	17
33	3.3.2	A heuristic packing relation	18
34	4	Exponent shifts, persistences and Betti number distributions	19
35	4.1	Amplitude redistribution-induced exponents shifts	19
36	4.2	Persistence distributions	21
37	4.3	Betti numbers as a consistency check	21
38	5	Conclusions	23
39	A	The mathematics of persistent homology	24
40	A.1	Relevant notions from algebraic topology	24
41	A.2	The construction and structure of persistent homology groups	25
42	B	The computational pipeline	26
43	C	Packing relation from bounded total persistence	27
44	D	Relating persistent homology exponents to correlation function expo-	
45		nants	27
46	E	Details on the nonrelativistic Bose gas simulations	28
47	F	2-point correlation function results in the infrared	28
48	G	Numerical convergence of persistent homology observables	30
49	H	Numerical protocol to extract persistent homology scaling exponents	33
50		References	34

51

52

53 1 Introduction

54 Emanating from algebraic topology and Morse theory, the applied mathematics branch
55 of topological data analysis has gained considerable attention over the past two decades,
56 accompanied by far-reaching theoretical and computational developments [1, 2]. Using
57 tools from abstract algebra, algebraic topology offers powerful and versatile methods to
58 globally study the structure of topological spaces by means of homology groups. Derived
59 from the latter, quantities such as Betti numbers prominently appear in this context
60 [3]. Resolving homological structure on different scales, hierarchically, in topological data
61 analysis the notion of persistent homology makes a multi-scale description of topological
62 structure contained in point cloud data possible [4–6]. To accomplish this, simplicial
63 complexes such as so-called Čech complexes, Vietoris-Rips complexes or alpha shapes
64 [7, 8] are employed. Besides the mathematical investigations on persistent homology, very
65 fruitful applications to physical systems include studies in astrophysics and cosmology

66 [9–12], physical chemistry [13], amorphous materials [14], quantum algorithms [15–19]
67 and the theory of quantum phase space [20].

68 In this work, we propose persistent homology observables for the analysis of the dy-
69 namics of quantum many-body systems. As a prototype application, we consider a Bose
70 gas far from equilibrium. While there are many different ways of driving a Bose gas away
71 from equilibrium, it has recently been demonstrated experimentally that the subsequent
72 relaxation dynamics can exhibit universal properties that are insensitive to the details of
73 the initial conditions and system parameters [21–23]. Theoretical results based on field
74 correlation functions indicate that vastly different systems far from equilibrium may share
75 very similar universal scaling properties, ranging from post-inflationary dynamics in the
76 early universe [24,25], and ultra-relativistic collision experiments with heavy nuclei [26–28],
77 to ultra-cold quantum gases in the laboratory [29,30]. In particular, quantum as well as
78 classical statistical field theories appear to belong to the same nonthermal universality
79 class [31]. These similarities have to be tested against refined analysis and classification
80 schemes. We will exploit the multi-scale topological information encoded in a family of
81 alpha complexes and in associated persistent homology groups in order to analyze self-
82 similar scaling dynamics in position space variables.

83 More precisely, serving as a numerical testbed, we apply topological data analysis
84 techniques to the dynamics of the single-component nonrelativistic Bose gas in two spatial
85 dimensions, described by the time-dependent Gross-Pitaevskii equation with quantum ini-
86 tial conditions. The latter exhibits a rich phenomenology far from equilibrium, including
87 various nonthermal fixed points associated to regimes of weak and strong wave turbu-
88 lence [32–34]. Focussing on the nonperturbative strong wave turbulence regime, a vertex-
89 resummed two particle-irreducible expansion scheme has been successfully employed to
90 obtain analytical predictions for relevant scaling exponents [31,35]. The existence of cor-
91 responding nonthermal fixed points has been confirmed by means of numerical lattice simu-
92 lations [36]. In addition, the infrared nonthermal fixed point can be dominated by vorticial
93 excitations interacting anomalously with each other via 3-vortex interactions [36,37], that
94 is, altering the universal scaling behavior. It has been conjectured that this anomalous
95 vortex kinetics is associated to the formation of Onsager vortex clusters out of equilib-
96 rium via evaporative heating [38,39]. Recently, experimental evidence for scale-invariant
97 dynamics and Onsager’s model has been reported [40,41].

98 Guided by numerical results for the two-dimensional Bose gas, we reveal that at late
99 times far from equilibrium persistent homology observables can show self-similar scaling
100 characteristic to a nonthermal fixed point. We discover a continuous spectrum of dynamical
101 scaling exponents, depending on a filtration parameter to construct point clouds, which
102 provides a refined classification of nonequilibrium universal phenomena. The existence of
103 such a scaling exponent spectrum seems to indicate scaling species mixing, in our case
104 between the strong wave turbulence and the anomalous vortex kinetics nonthermal fixed
105 points present in the infrared of the particular Bose gas. The analysis is supplemented
106 by a thorough investigation of accompanying subtleties of the chosen persistent homology
107 approach such as amplitude redistribution-induced exponent shifts.

108 On the theoretical side, we define persistent homology observables. We introduce the
109 notion of a persistence pair distribution and its statistical asymptotics in order to infer
110 self-similar behavior of the latter. We reveal that the appearing scaling exponents probe
111 the geometry at hand, as indicated by a packing relation derived in this study.

112 This publication is structured as follows. With the Bose gas simulations at hand,
113 we introduce and study point clouds and persistent homology groups in Sec. 2. Redis-
114 covering self-similarity, this exploration culminates in the existence of a scaling exponent
115 spectrum. In Sec. 3 we carry out the construction of persistent homology observables

116 in the classical-statistical framework, introduce the asymptotic persistence pair distribu-
 117 tion and related geometric quantities and investigate a corresponding self-similar scaling
 118 ansatz. We discuss amplitude redistribution-induced exponent shifts, persistences and
 119 Betti number distributions in Sec. 4. Finally, in Sec. 5 we summarize, draw conclusions
 120 and issue an outlook.

121 2 Persistent homology in a Bose gas

122 Focussing on lattice simulations of the nonrelativistic Bose gas in two dimensions, we
 123 introduce a simple approach to construct point clouds, namely as sublevel sets of field
 124 amplitudes. Given such point clouds, a rather intuitive sketch of the construction of
 125 alpha complexes and persistent homology groups is provided. In corresponding far-from-
 126 equilibrium simulations we discover growing geometric structures and self-similar scaling
 127 at large length scales and late times. In particular, the existence of a scaling exponent
 128 spectrum is revealed. By means of the mixing of scaling dynamics species we offer a
 129 possible route to explain this finding.

130 2.1 Simulation prerequisites

131 The nonrelativistic Bose gas can be described by complex scalar fields $\psi(t, \mathbf{x})$ depending on
 132 time and space, in numerical simulations restricted to a spatial lattice and time-evolved in
 133 discrete time-steps. We focus on the overoccupied regime, in which the classical-statistical
 134 approximation is suitable [31]. Accordingly, at initial time $Qt = 0$ a number k of classi-
 135 cal field configurations is sampled from a Gaussian ensemble, computing their individual
 136 subsequent dynamics according to the time-dependent Gross-Pitaevskii equation. In the
 137 classical-statistical approximation expectation values of an observable are computed as
 138 ensemble-averages of the observable evaluated for individual field configurations. With
 139 the momentum denoted by \mathbf{p} , initial field configurations fulfill

$$\frac{1}{2} \int d^2x e^{-i\mathbf{p}\mathbf{x}} \langle \psi(0, \mathbf{x}) \psi^*(0, \mathbf{0}) + \psi(0, \mathbf{0}) \psi^*(0, \mathbf{x}) \rangle = \frac{50}{2mgQ} \Theta(Q - |\mathbf{p}|), \quad (1)$$

140 that is, initially, the Fourier-transformed statistical two-point correlation function — the
 141 occupation number spectrum — is described in terms of a momentum scale Q . Unlike a
 142 system in thermal equilibrium, where the typical occupancy is of order unity at a character-
 143 istic temperature scale T , here we consider a nonequilibrium system where the occupancy
 144 at a given characteristic scale Q is much higher than unity. Any dimensionful physical
 145 quantity will be given in units of Q . We set the mass $m/Q = 8$ and coupling $Qg = 0.0625$
 146 throughout this work. Outside the box, no ‘quantum-half’ is taken into account and no
 147 initial condensate is specified. Spatial coordinates are restricted to a square lattice, Λ ,
 148 consisting of a regular grid of N^2 points within a volume L^2 with periodic boundary con-
 149 ditions. Throughout this work, the lattice spacing reads $Qa = 0.0625$, the number of
 150 lattice sites $N = 1536$, such that

$$\Lambda = \{(an_1, an_2) \mid n_1, n_2 \in \{0, \dots, N - 1\}\}. \quad (2)$$

151 If not stated differently, we average over $k = 72$ classical-statistical realizations to compute
 152 classical-statistical expectation values. For further details on the numerical simulations
 153 we refer to Appendix E.

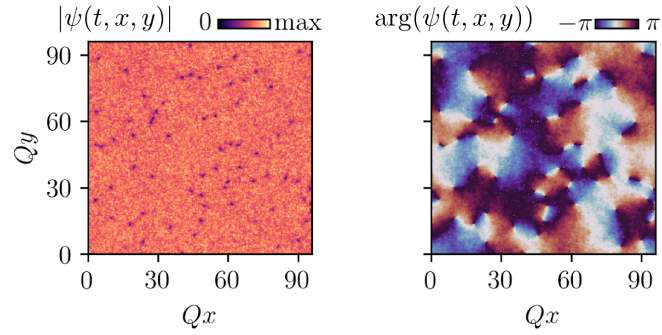


Figure 1: Amplitudes (left) and phases (right) of an example field configuration at time $Qt = 3750$.

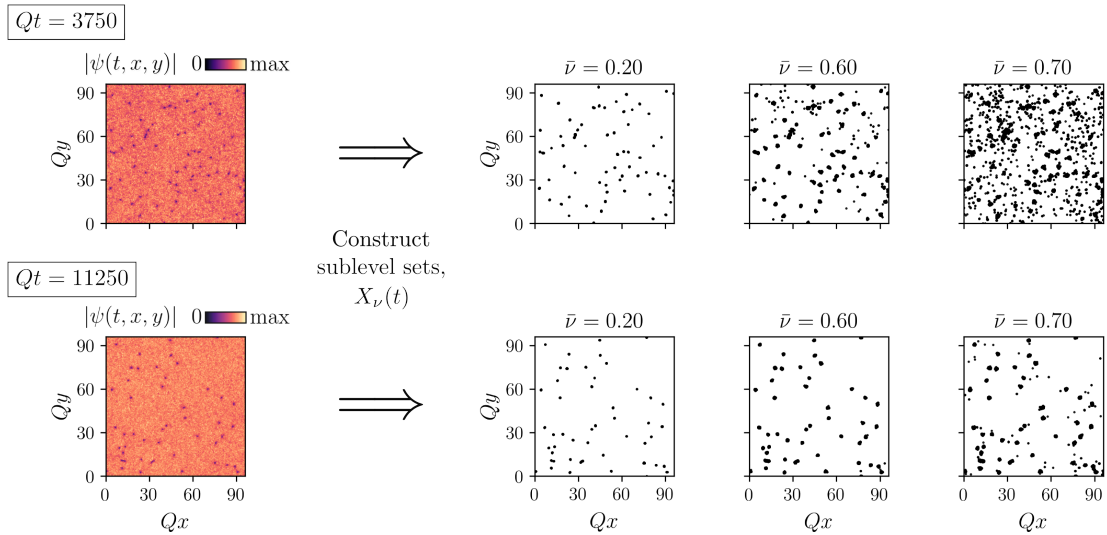


Figure 2: Amplitudes of an example field configuration and corresponding point clouds. First column from the left: Spatially-resolved field amplitudes, $|\psi(t, x, y)|$. Second to fourth column: Point clouds $X_\nu(t)$ for the different $\bar{\nu}$ -values indicated. First row: $Qt = 3750$. Second row: $Qt = 11250$.

154 2.2 Phenomenology of point clouds

155 Given a classical-statistical field realization $\psi(t, \mathbf{x})$, an immense freedom of choice exists
 156 in constructing point clouds, which are, generally speaking, finite sets of points in an
 157 arbitrary Euclidean space. We define a *filtration function* f to be a map from \mathbb{C} to \mathbb{R} used
 158 to generate point clouds as subsets of the lattice Λ . We may construct point clouds as
 159 sublevel sets of $f(\psi(t, \cdot))$, that is, at time Qt define them as $\{\mathbf{x} \in \Lambda \mid f(\psi(t, \mathbf{x})) \in (-\infty, \nu]\}$
 160 for a *filtration parameter* ν . In this work, point clouds are generated as sublevel sets of
 161 the field amplitude, thus defining

$$X_\nu(t) := \{\mathbf{x} \in \Lambda \mid |\psi(t, \mathbf{x})| \leq \nu\}. \quad (3)$$

162 By means of this definition, the ensemble of classical-statistical field realizations translates
 163 for each time Qt into an ensemble of point clouds. Numerically, we specify the filtration
 164 parameter ν by means of the dimensionless variant $\bar{\nu}$,

$$\bar{\nu} := \nu / \langle |\psi(t=0)| \rangle_{\text{vol}}, \quad (4)$$

165 with the volume-averaged initial field amplitude

$$\langle |\psi(t=0)| \rangle_{\text{vol}} = \frac{1}{N^2} \sum_{\mathbf{x} \in \Lambda} |\psi(t=0, \mathbf{x})|. \quad (5)$$

166 We want to emphasize that in experiments with cold atoms optical density images
 167 as given by the square of the amplitudes displayed in Fig. 1 and used in the filtration
 168 protocol, Eq. (3), form a typical observational quantity and can be easily accessed via
 169 absorption images. Varying the filtration parameter $\bar{\nu}$ amounts to measurements up to the
 170 square root of corresponding condensate densities, highlighting the physical significance
 171 of the employed point cloud construction via Eq. (3).

172 Simulating on a spatial square lattice with constant lattice spacing, we want to stress
 173 that to obtain point clouds by means of Eq. (3), to compute alpha complexes and to
 174 evaluate persistent homology groups only the finiteness of the lattice is crucial. Else,
 175 $X_\nu(t)$ might consist of infinitely many points. The construction of persistent homology
 176 groups, carried out in Sec. 2.3, is robust against perturbations of the lattice points¹.
 177 This renders the microscopic form of the lattice irrelevant for later numerical persistent
 178 homology results. The constant lattice spacing and finite lattice volume solely amount to
 179 a smallest and a largest length scale amenable to the investigated real-time dynamics.

180 In Fig. 1 amplitudes and phases of a single classical-statistical field realization are
 181 displayed. One may first note from the amplitudes on the left that in position space
 182 the system comprises two major components: fluctuations in the bulk around a mean
 183 amplitude value larger than zero and distinct minima with minimum values near to zero.
 184 While phases differ locally only slightly in regions where minima are absent, around each
 185 minimum phase windings with shifts of $\pm 2\pi$ occur. Thus, the minima can be identified
 186 with elementary vortex nuclei.

187 In Fig. 2 at two different times we show spatially-resolved amplitudes and a variety of
 188 point clouds computed from a single classical-statistical field realization. In point clouds
 189 $X_\nu(t)$ as defined by Eq. (3), at both times visualized we find clear manifestations of
 190 the aforementioned two components appearing in amplitudes. Having approximately zero
 191 amplitude at the center of their nuclei, vortices dominate the point clouds $X_\nu(t)$ for small

¹Mathematically, in a number of ways persistent homology groups are stable against perturbations of corresponding input, cf. inter alia Refs. [42, 43]. This implies, that if points in $X_\nu(t)$ are altered slightly, then persistence diagrams of the sequence of alpha complexes of $X_\nu(t)$ change only slightly, too.

192 filtration parameters such as $\bar{\nu} = 0.2$. In the limit of $\bar{\nu} \rightarrow 0$ point clouds actually comprise
 193 mostly vortex positions themselves, although the presence of points originating from bulk
 194 density fluctuations cannot be excluded. Described by point vortex models, for this reason
 195 the low- $\bar{\nu}$ limit can be associated to the incompressible limit of the theory. Increasing $\bar{\nu}$,
 196 in point clouds points first accumulate around vortex nuclei but at moderately high values
 197 such as $\bar{\nu} = 0.6$ also occur in the bulk. The higher $\bar{\nu}$ gets, the denser point clouds become,
 198 reducing the average distance between points. Hence, studying point clouds at different
 199 $\bar{\nu}$ -values effectively probes the system on different length scales.

200 Comparing the two times displayed, we note that the number of vortices decreases with
 201 time, or, equivalently, the average inter-vortex distance increases. In Fig. 2 point clouds
 202 at $\bar{\nu} = 0.2$ reflect this behavior, becoming sparser in the course of time. Similarly, at
 203 higher values of $\bar{\nu}$ the density of points in point clouds decreases in regions where vortices
 204 are absent. All this indicates that in the temporal regime of the displayed times geometric
 205 structures in point clouds continuously grow at large length scales.

206 Yet, one may notice that for $\bar{\nu} = 0.6$ and $\bar{\nu} = 0.7$ the number of points in the bulk
 207 decreases faster compared to the decline in vortex numbers. This provides a first hint at
 208 the presence of different components, whose dynamics differ in terms of “speed”.

209 2.3 An introduction to persistent homology

210 To obtain a robust quantitative means of the topological structure present in a point cloud
 211 $X_\nu(t)$, persistent homology can be employed. Aiming at an intuitive treatment, with a
 212 point cloud $X_\nu(t)$ at hand as it appears in the Bose gas simulations we introduce relevant
 213 notions from computational topology. From given input data we first define the Delaunay
 214 complex and a notion of the size of a simplex. The so-called Delaunay radius function
 215 can then be used to construct a nested sequence of subcomplexes, called alpha complexes,
 216 whose persistent homology groups form our objects of interest and eventually provide
 217 multi-scale information on the topological structure of the input point cloud. While we
 218 carry out constructions in two spatial dimensions here, they generalize easily to higher
 219 dimensions.

220 In Appendix A we rigorously introduce relevant fundamental algebraic topology no-
 221 tions and discuss the mathematical construction of persistent homology groups. For a
 222 general introduction to algebraic topology we refer to Ref. [3]; for a thorough introduction
 223 to computational topology the interested reader may consult Refs. [2, 6], for instance.

224 2.3.1 Alpha complexes

225 Let $X_\nu(t)$ be a point cloud as defined by Eq. (3). We construct persistent homology
 226 groups from a nested family of simplicial complexes. A *simplicial complex* \mathcal{S} on $X_\nu(t)$
 227 comprises the set $X_\nu(t)$ together with a collection \mathcal{S} of subsets of $X_\nu(t)$. The defining
 228 property of a simplicial complex is that for all points $x \in X_\nu(t)$, the vertex $\{x\} \in \mathcal{S}$, and
 229 if $\tau \subseteq \sigma \in \mathcal{S}$, then $\tau \in \mathcal{S}$, i.e. \mathcal{S} is closed under taking subsets. The elements of \mathcal{S} are
 230 called its *simplices*. Combinatorially, this structure allows for the computation of various
 231 descriptors of its topology, in particular the homology groups of \mathcal{S} . We deliver details in
 232 Appendix A.1.

233 Let us construct the particular type of simplicial complexes employed in this work:
 234 alpha complexes. Clearly, for any three points in $X_\nu(t)$ that do not lie on a single straight
 235 line, a unique circumsphere passing through the points exists. Any two points can be
 236 trivially identified with a zero-dimensional circumsphere. We shall assume that the points
 237 in $X_\nu(t)$ are in general position. This excludes, for example, the possibility that three or

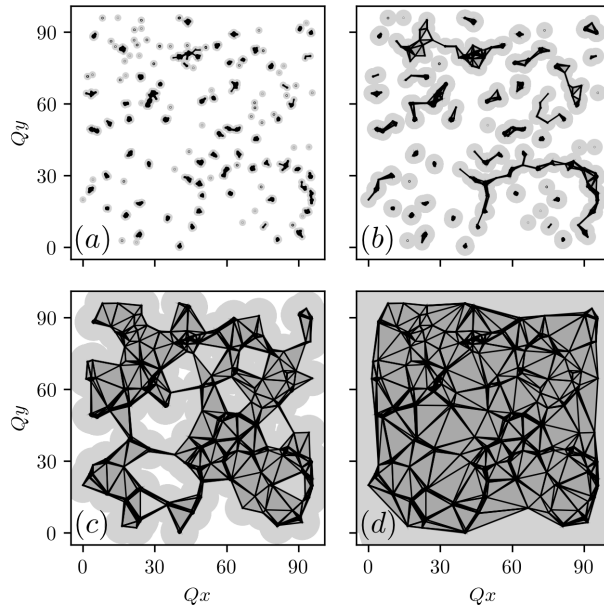


Figure 3: Alpha complexes of various radii Qr of the point cloud $X_\nu(Qt = 3750)$ for $\bar{\nu} = 0.6$ as displayed in Fig. 2. Panel (a): $Qr = 1.0$. Panel (b): $Qr = 3.0$. Panel (c): $Qr = 7.0$. Panel (d): $Qr = 20.0$.

238 more points are collinear or that four or more points lie on a single circle². Then, any
 239 two or three points in $X_\nu(t)$ have a unique zero- or one-dimensional circumsphere passing
 240 through these points, respectively³. We call a circumsphere empty, if all points of $X_\nu(t)$
 241 lie on or outside the sphere.

242 The *Delaunay complex*, $\text{Del}(X_\nu(t))$, can be defined to consist of all points in $X_\nu(t)$ as
 243 well as those edges and triangles whose circumspheres are empty [45]. Speaking about
 244 terminology, a point is a zero-dimensional simplex, an edge between two points is a one-
 245 dimensional simplex and a triangle is a two-dimensional simplex. As described in Ref. [44],
 246 for point clouds in general position this procedure yields that the corresponding Delaunay
 247 complex is a simplicial complex, allowing for the construction of homology groups as
 248 described intuitively below.

249 The *Delaunay radius function* $\text{Rad} : \text{Del}(X) \rightarrow [0, \infty)$ is defined to map every simplex
 250 to the smallest radius of all its empty circumspheres. Intuitively, it provides a measure
 251 for the size of a simplex. In Fig. 3d the Delaunay complex of an example point cloud
 252 $X_\nu(t)$ as it appears in the Bose gas simulations is displayed for $\bar{\nu} = 0.6$. Note that
 253 simplices of different Delaunay radii are visually of distinct dominance, typically. Smaller
 254 simplices appear foremost around local accumulations of points, while simplices of larger
 255 radii mainly make up the large-scale structure between them.

256 Let $Qr \in [0, \infty)$ be some length scale. Capturing appearing structures of particular
 257 sizes, from the Delaunay radius function we finally construct *alpha complexes*⁴ as its
 258 sublevel sets,

$$\alpha_r(X_\nu(t)) := \{\sigma \in \text{Del}(X_\nu(t)) \mid \text{Rad}(\sigma) \leq Qr\}. \quad (6)$$

²While different definitions of general position exist across the literature, we employ the one used in Ref. [44].

³In general spatial dimension d this would amount to any $2 \leq j \leq d + 1$ points x_{i_1}, \dots, x_{i_j} having a unique $(j - 2)$ -dimensional circumsphere passing through all these points.

⁴Generically, alpha complexes are simplicial subcomplexes of the Delaunay complex [6].

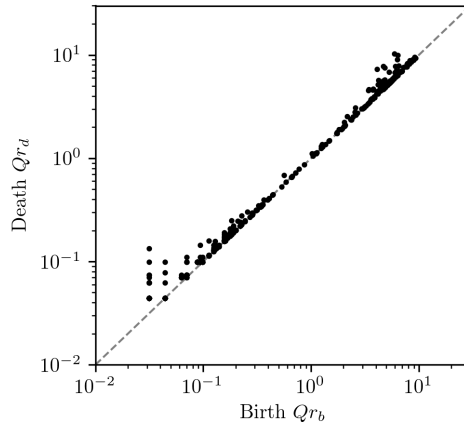


Figure 4: Persistence diagram of one-dimensional homology classes for the sequence of alpha complexes partially displayed in Fig. 3, $\text{Dgm}_1(X_\nu(t))$.

259 For all $0 \leq r \leq s$ we find $\alpha_r(X_\nu(t)) \subseteq \alpha_s(X_\nu(t))$. To this end, we obtain what is
 260 called a *filtration* of the Delaunay complex $\text{Del}(X_\nu(t))$, that is, a nested sequence of alpha
 261 complexes little by little filling out all $\text{Del}(X_\nu(t))$,

$$\emptyset \subseteq \alpha_{r_1}(X) \subseteq \dots \subseteq \alpha_{r_\kappa}(X) = \text{Del}(X), \quad (7)$$

262 with $r_i \leq r_j$ for all $i < j$.

263 Again referring to the example point cloud $X_\nu(t)$, in Fig. 3 corresponding alpha
 264 complexes of different radii Qr are displayed. Note that at a small radius such as $Qr = 1.0$
 265 the alpha complex mainly reflects the local accumulations of points in $X_\nu(t)$. Topological
 266 structures such as holes are of tiny size and each connected component loosely corresponds
 267 to a local accumulation of points. Besides seemingly random connected structures, at
 268 intermediate radii comparably large-scale holes appear in the alpha complexes, such as
 269 visible in the $Qr = 7.0$ alpha complex displayed in Fig. 3c. At even larger radii, the
 270 full Delaunay complex is recovered, in accordance with Eq. (7). Leading to the notion
 271 of persistent homology, it is a crucial insight that independent connected components
 272 disappear at a certain radius, merging with other components, and that holes only appear
 273 in alpha complexes of a certain radius and disappear again at a higher radius.

274 2.3.2 Persistent homology and the persistence diagram

275 This intuitive picture can be turned into a mathematical concept: persistent homology.
 276 In Appendix A.2, we provide a more rigorous introduction to it, while here we focus on
 277 capturing its intuitive essence.

278 Alpha complexes of zero radius only consist of the vertices, that is, all points contained
 279 in the point cloud $X_\nu(t)$. Certainly, the number of connected components in the alpha
 280 complex of zero radius equals the cardinality of $X_\nu(t)$. Increasing the radius, at a certain
 281 value a first edge between two vertices appears in the alpha complex. A previously inde-
 282 dependent connected component *dies*. We call the minimum radius at which it is not present
 283 anymore in the corresponding alpha complex its *death radius*. The radius rising further,
 284 more and more connected components die, merging into a larger and larger complex. From
 285 a certain radius onwards, only one connected component is present in the corresponding
 286 alpha complexes. In Fig. 3 the process of connected components merging one by one into
 287 larger complexes can be observed as the sequence of alpha complexes is traversed towards
 288 larger radii.

289 With radii increasing, in the sequence of alpha complexes holes begin to appear as is
 290 clearly visible in Figs. 3b and 3c. The minimum radius at which an independent hole
 291 first appears in the sequence of alpha complexes is called its *birth radius*. We say that it
 292 is *born* at its birth radius. Successively, a given hole is filled out with triangles in alpha
 293 complexes of rising radii, until from its *death radius* onwards the hole vanishes, being fully
 294 filled.

295 In fact, in simplicial homology independent connected components are described by
 296 *zero-dimensional homology classes* and independent holes by *one-dimensional homology*
 297 *classes*. If the point clouds of interest lived in a higher-dimensional Euclidean space,
 298 one could continue analogously to describe the birth and death of higher-dimensional
 299 homology classes. This includes, for instance, independent enclosed voids represented
 300 by two-dimensional homology classes. Homology classes of dimension ℓ , appearing and
 301 disappearing again as the sequence of alpha complexes is traversed, are collected in groups,
 302 the ℓ -th *persistent homology groups*, cf. Appendix A.2.

303 Summarizing the structure of ℓ -th persistent homology groups, the ℓ -th *persistence*
 304 *diagram* $\text{Dgm}_\ell(X_\nu(t))$, is defined to contain all birth radius-death radius pairs (r_b, r_d) of
 305 ℓ -dimensional homology classes appearing in the sequence of alpha complexes of $X_\nu(t)$,
 306 taking respective multiplicities into account for coinciding such pairs⁵. In Fig. 4 the
 307 persistence diagram of one-dimensional homology classes is displayed for the sequence of
 308 alpha complexes partially shown in Fig. 3. Certainly, in a persistence diagram all points
 309 lie above the diagonal $r_b = r_d$, since the death of any homology class happens at a higher
 310 radius than its birth. We find that in the bottom-left of the diagram an accumulation
 311 of pairs is present, corresponding to comparably small one-dimensional homology classes
 312 (holes). The partly vertical alignment of points can be attributed to the homogeneity of the
 313 square lattice, on which $X_\nu(t)$ resides. In addition, we find a second accumulation of pairs
 314 in the top-right of the diagram, corresponding to larger-size one-dimensional homology
 315 classes in corresponding alpha complexes. On these length scales birth and death radii
 316 are approximately independent from the microscopic lattice geometry.

317 2.3.3 Statistical measures: birth and death radii distributions

318 To obtain expectation values in the classical-statistical framework, ensemble-averages of
 319 quantities describing persistence diagrams of individual classical-statistical realizations
 320 are required. Persistence diagrams themselves are difficult objects to study statistically.
 321 Without modifications not even a statistical average can be defined unambiguously. Nev-
 322 ertheless, there exist multifarious quantities suitable for a statistical treatment [46]. We
 323 introduce two of these here, postponing the general description to Sec. 3.1. We explicitly
 324 construct classical-statistical ensemble-averages. To this end, let $X_\nu^{(i)}(t)$, $i \in \mathbb{N}$, be an
 325 ensemble of point clouds, all constructed from individual field realizations according to
 326 Eq. (3). Denote by $D_\ell^{(i)}(t) := \text{Dgm}_\ell(X_\nu^{(i)}(t))$ the ℓ -th persistence diagram of the i -th
 327 such point cloud. Let $\sigma > 0$ be a constant. We define the expectation values of the ℓ -th

⁵The persistence diagram is a finite multiset of points in \mathbb{R}^2 , also taking respective multiplicities into account.

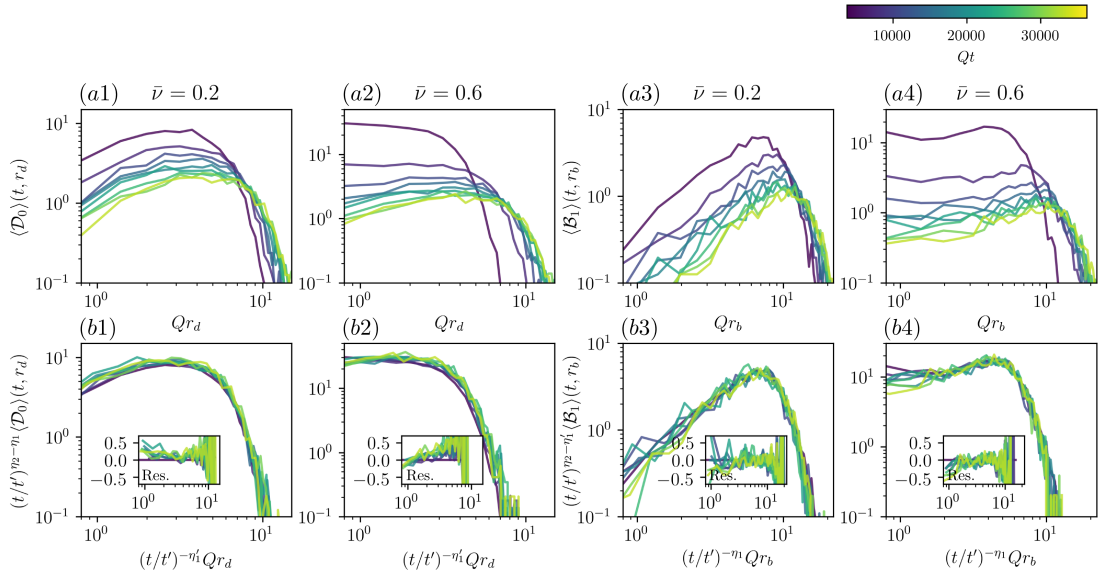


Figure 5: Birth and death radii distributions in the infrared. Columns 1 and 2: Death radii of zero-dimensional homology classes. Columns 3 and 4: Birth radii of one-dimensional homology classes. Individual columns show data for the indicated filtration parameter, $\bar{\nu}$. Row 1: unrescaled distributions. Row 2: rescaled distributions. The employed time-dependent scaling exponents are displayed in Fig. 7.

328 *distribution of birth radii and the ℓ -th distribution of death radii as*

$$\langle \mathcal{B}_\ell \rangle(t, r_b) = \lim_{k \rightarrow \infty} \frac{1}{k} \sum_{i=1}^k \sum_{(r'_b, r'_d) \in D_\ell^{(i)}(t)} \frac{1}{2\pi\sigma^2} \exp\left(-\frac{(r_b - r'_b)^2}{2\sigma^2}\right), \quad (8a)$$

$$\langle \mathcal{D}_\ell \rangle(t, r_d) = \lim_{k \rightarrow \infty} \frac{1}{k} \sum_{i=1}^k \sum_{(r'_b, r'_d) \in D_\ell^{(i)}(t)} \frac{1}{2\pi\sigma^2} \exp\left(-\frac{(r_d - r'_d)^2}{2\sigma^2}\right), \quad (8b)$$

329 respectively. Note that these distributions are statistically well-behaved, such that aver-
 330 ages and the denoted limits exist [47]. The parameter σ is chosen sufficiently large, such
 331 that numerical outcomes are independent from its particular value.

332 2.4 Growing geometric structures in persistent homology

333 Using a computational topology pipeline as described in Appendix B, we can numerically
 334 investigate birth and death radii distributions for different filtration parameters $\bar{\nu}$ in
 335 the aforementioned Bose gas simulations. For large length scales, in Fig. 5 death radii
 336 distributions of zero-dimensional homology classes and birth radii distributions of one-
 337 dimensional homology classes are displayed at times between $Qt = 3750$ and $Qt = 35625$.
 338 Zero-dimensional persistent homology classes are always born at radius $Qr_b = 0$, turning
 339 the distribution of birth radii of zero-dimensional homology classes trivial. The occurring
 340 oscillations in distributions are due to statistical uncertainties, being computed from only
 341 a finite number of classical-statistical samples.

342 We first discuss unrescaled variants of the displayed distributions. It is important
 343 to note that in any of the distributions the maximum number of counts in birth and
 344 death radii distributions decreases with time. Simultaneously, the steep decline at largest
 345 radii in birth and death distributions constantly shifts to higher radii. Clearly, these are

346 manifestations of geometric structures in the system growing at large length scales as
 347 conjectured in Sec. 2.2 from the point clouds themselves. Beyond this, the approximately
 348 constant form of the distributions already provides a first hint at self-similar dynamics.

349 In first death radii distributions a clear peak is visible, in particular for $\bar{\nu} = 0.2$ as
 350 displayed in Fig. 5, panel (a3). Point clouds for small $\bar{\nu}$ -values being dominated by
 351 accumulations of points around vortex nuclei, we expect this distinguished length scale
 352 to provide a measure for the average inter-vortex distance. At higher $\bar{\nu}$ -values such as
 353 $\bar{\nu} = 0.6$ the peak is blurred by means of bulk points entering corresponding point clouds.

354 2.5 Unveiling a spectrum of scaling exponents

355 Motivated by the approximately constant form of the distributions displayed in Fig. 5, we
 356 examine whether they can be consistently described by a self-similar scaling ansatz. We
 357 say that birth and death radii distributions *scale self-similarly*, if exponents η_1, η'_1 and η_2
 358 exist, such that for all times t, t' ,

$$\langle \mathcal{B}_\ell \rangle(t, r_b) = (t/t')^{\eta'_1 - \eta_2} \langle \mathcal{B}_\ell \rangle(t', (t/t')^{-\eta_1} r_b), \quad (9a)$$

$$\langle \mathcal{D}_\ell \rangle(t, r_d) = (t/t')^{\eta_1 - \eta_2} \langle \mathcal{D}_\ell \rangle(t', (t/t')^{-\eta'_1} r_d). \quad (9b)$$

359 In Sec. 3.3 we deduce this particular form of scaling behavior from a scaling ansatz
 360 to a more general quantity that describes persistent homology groups, the asymptotic
 361 persistence pair distribution. Notice that in this scaling ansatz a possible dependence on
 362 the dimension ℓ of homology classes is neglected, supported by numerics.

363 Using the numerical protocol described in Appendix H, scaling exponents are extracted
 364 from birth and death radii distributions of one-dimensional homology classes. Given a time
 365 Qt_{\min} , birth and death radii distributions at times Qt_{\min} , $Qt_{\min} + 625$ and $Qt_{\min} + 1250$
 366 are fitted simultaneously against distributions at reference time $Qt' = 3750$. A measure
 367 for the quality of a self-similar description of the investigated distributions is provided by
 368 means of residuals. For instance, for the distribution of birth radii residuals at time Qt
 369 are computed as

$$\text{Res.}(\langle \mathcal{B}_\ell \rangle)(t, r_b) := \frac{(t/t')^{\eta'_1 - \eta_2} \langle \mathcal{B}_\ell \rangle(t', (t/t')^{-\eta_1} r_b)}{\langle \mathcal{B}_\ell \rangle(t, r_b)} - 1. \quad (10)$$

370 Indeed, distributions can be consistently rescaled by means of the scaling ansatz de-
 371 scribed in Eqs. (9a) and (9b). This can be deduced from Fig. 5 with residuals of rescaled
 372 distributions scattering approximately evenly around zero. Note that distributions of
 373 both zero- and one-dimensional homology classes can be consistently rescaled with the
 374 same triple of exponents, validating that in the scaling ansatz we neglected a possible
 375 ℓ -dependence. However, *filtration parameter- and time-dependent* scaling exponents are
 376 necessary for a successful rescaling.

377 In Fig. 6 we show the scaling exponents for a single minimum fitting time Qt_{\min} ,
 378 highlighting the size of error bars. Errors origin from a finite number of classical-statistical
 379 samples taken into account and from fitting uncertainties. For values of $\bar{\nu} \lesssim 0.4$ the
 380 displayed exponent values approximately lie around 0.2. A rise in values takes place
 381 for $\bar{\nu} \gtrsim 0.5$, up to a maximum value of approximately 0.8. Thus, we make the crucial
 382 observation that a *continuous spectrum* of scaling exponents exists, depending on the
 383 filtration parameter $\bar{\nu}$.

384 Within error bars η_1 equals η'_1 at all $\bar{\nu}$ -values investigated here. This provides numerical
 385 evidence for that birth and death radii show the same dynamics at large length scales. In
 386 addition, for all $\bar{\nu}$ -values analyzed $\eta_2/\eta_1 = 4$ within the indicated error bars. This relation

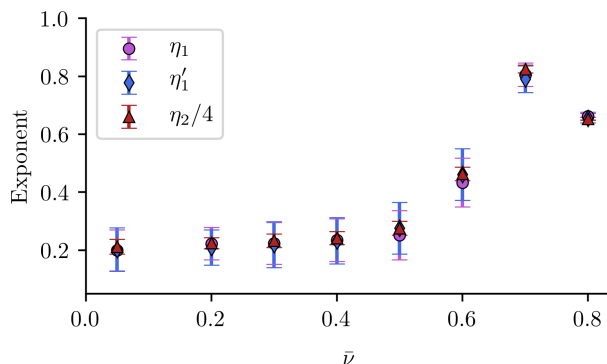


Figure 6: Persistent homology scaling exponents at $Qt_{\min} = 18750$.

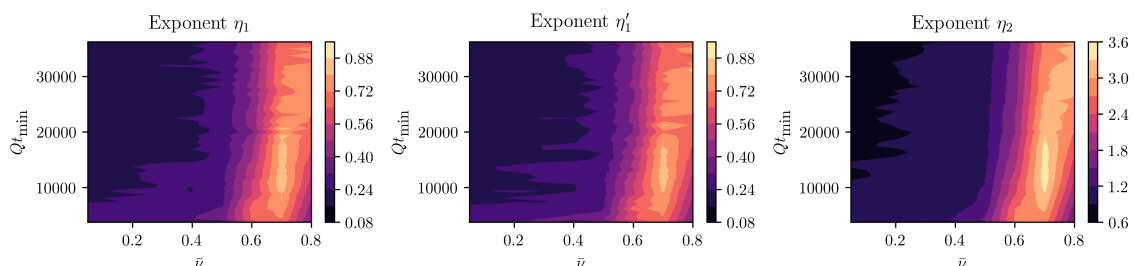


Figure 7: Persistent homology scaling exponents for different filtration parameters $\bar{\nu}$ and minimum fitting times Qt_{\min} .

387 results from the bounded packing of homology classes of a given size into the constant
 388 lattice volume, as shown in Sec. 3.3.2.

389 Comprehensively, results are summarized in Fig. 7, in which exponents are displayed
 390 in the full $(\bar{\nu}, Qt_{\min})$ -plane. The gradual shift of the peak in scaling exponents to higher
 391 $\bar{\nu}$ -values with increasing fitting time Qt_{\min} is a result of the redistribution of amplitude
 392 values with time, discussed in Sec. 4.1. The scattering of exponent values at larger $\bar{\nu}$ -values
 393 is due to statistical uncertainties.

394 2.6 Scaling species and exponents mixing conjecture

395 An observation such as the existence of a whole spectrum of scaling exponents at large
 396 length scales requires an explanation. We conjecture that its appearance is linked to
 397 different dynamical scaling species occurring in the infrared of the two-dimensional Bose
 398 gas.

399 First, note that momenta in the infrared regime correspond to large length scales.
 400 Hence, if infrared dynamics is visible in quantities describing the persistent homology of
 401 alpha complexes, it will show at correspondingly large birth and death radii. Vice versa,
 402 if ultraviolet physics is visible in persistent homology, it will show up at comparably small
 403 birth and death radii. To this end, we identify the regime of large birth and death radii
 404 in their distributions with the infrared regime of the system. This offers the possibility of
 405 linking aforementioned results to known momentum space dynamics of physical quantities.

406 In addition, for positive scaling exponents $\eta_1 = \eta'_1$ and η_2 the scaling ansatz described
 407 by Eqs. (9a) and (9b) corresponds to a blow-up of length scales as a power-law with
 408 exponent η_1 , as we detail in Sec. 3.3. Hence, a comparison of the exponent η_1 with scaling

409 exponents appearing in power-laws of further physical length scales is reasonable.

410 We restrict the following discussion to η_1 . For $\bar{\nu} \lesssim 0.4$, the exponent η_1 meets the
 411 value of $1/5$ associated to the anomalous vortex kinetics nonthermal fixed point [36, 41]
 412 and confirmed by the self-similar dynamics of occupation number spectra in the given
 413 simulations, cf. Appendix F. Point clouds, alpha complexes as well as birth and death
 414 radii distributions reflect the occurring vortex dynamics for small $\bar{\nu}$, correspondingly. This
 415 is in accordance with the observation made in Sec. 2.2 that for $\bar{\nu} \lesssim 0.4$ point clouds mainly
 416 comprise accumulations of points around vortex nuclei.

417 The exponent η_1 increases with $\bar{\nu}$ up to maximum values of between 0.7 and 0.9
 418 depending on Qt_{\min} , cf. Fig. 7 — a value which is significantly different from $1/5$. We
 419 take a small detour to provide a physical interpretation for this phenomenon.

420 Collectively, the vortices show anomalous kinetics and dominate point clouds at low
 421 $\bar{\nu}$ -values: $\eta_1(\bar{\nu} = 0.05) \approx 0.2$. It is well-known, however, that the two-dimensional nonrel-
 422 ativistic Bose gas not only exhibits the anomalous vortex kinetics nonthermal fixed point
 423 with $\beta = 0.2$, but also incorporates strong wave turbulence characterized by $\beta = 0.5$
 424 [31, 36, 41, 48], β denoting the corresponding scaling exponent in a correlation function
 425 scaling ansatz, cf. Eq. (43) in Appendix F. If the vortices were absent or coupled strongly
 426 to sound excitations in the bulk, only self-similar scaling with $\beta = 0.5$ would be visible, as
 427 argued for in Ref. [36]. Motivated by this, we infer that in the configurations investigated
 428 it is sound excitations in the bulk that reflect strong wave turbulence. Correspondingly, if
 429 bulk points enter point clouds, then birth and death radii distributions might show scaling
 430 behavior deviating from $\eta_1 = 0.2$. As can be seen in Figs. 2, 6 and 7 this is the case for
 431 growing $\bar{\nu}$ -values and explains the increase of η_1 . With this admittedly loose association
 432 of bulk points to strong wave turbulence and vortex nuclei points to anomalous vortex
 433 kinetics in mind, we refer to the underlying phenomenon as *scaling species mixing* in point
 434 clouds.

435 Yet, the maximum value of $\eta_1(\nu)$ exceeds 0.5 significantly for all Qt_{\min} . A heuristic
 436 geometric explanation proceeds as follows. Restrict to the dynamics of a single classical-
 437 statistical field configuration and corresponding point clouds $X_\nu(t)$. Let $Y_\nu(t) \subseteq X_\nu(t)$
 438 be associated to anomalous vortex kinetics and $Z_\nu(t) \subseteq X_\nu(t)$ associated to strong wave
 439 turbulence in the bulk, such that $X_\nu(t) = Y_\nu(t) \cup Z_\nu(t)$. The alpha complexes of $X_\nu(t)$,
 440 $\alpha_r(X_\nu(t))$, however, do not simply decay into $\alpha_r(Y_\nu(t))$ and $\alpha_r(Z_\nu(t))$. Instead, depending
 441 on the precise arrangements of points in $Y_\nu(t)$ and $Z_\nu(t)$, there may be a lot of simplices
 442 contained in $\alpha_r(X_\nu(t))$ which incorporate points of both $Y_\nu(t)$ and $Z_\nu(t)$. In addition,
 443 simplices that only consist of points in $Y_\nu(t)$ or $Z_\nu(t)$ can be very different from the ones
 444 in $\alpha_r(Y_\nu(t))$ and $\alpha_r(Z_\nu(t))$. The construction of alpha complexes from $Y_\nu(t)$ and $Z_\nu(t)$ is
 445 a highly nonlinear process. Birth and death radii distributions can reflect this behavior.

446 3 Persistent homology observables and self-similarity

447 In this section we embed alpha complexes and persistent homology descriptors into the
 448 classical-statistical regime of quantum field theory (QFT). By means of functional sum-
 449 maries of persistence diagrams, this leads to the definition of persistent homology observ-
 450 ables. In quite a few examples of these the same integral kernel appears, which we call
 451 the asymptotic persistence pair distribution. This paves the way to a self-similar scaling
 452 approach for the asymptotic persistence pair distribution, whose outgrowths for birth and
 453 death radii distributions are given by Eqs. (9a) and (9b). In Sec. 2.5 this particular
 454 scaling behavior has been shown to describe simulation outcomes well.

455 3.1 Persistent homology observables via functional summaries

456 Naturally, studying persistent homology in QFT requires a statistical treatment. Persist-
 457 tence diagrams themselves, however, do not admit a clear notion of averages [46]. Instead,
 458 we propose to focus on so-called functional summaries, providing general statistically well-
 459 behaved descriptors of persistence diagrams. In Sec. 3.2 we reveal that the investigated
 460 birth and death radii distributions given by Eqs. (8a) and (8b) are corresponding exam-
 461 ples.

462 Let \mathcal{D} be the space of persistence diagrams, that is, the space of finite multisets of
 463 points within $\{(r_b, r_d) \in [0, \infty)^2 \mid r_d \geq r_b\}$. Let \mathcal{F} be a collection of functions, $f : \Omega \rightarrow \mathbb{R}$
 464 for all $f \in \mathcal{F}$, Ω being a compact space. Following Ref. [47], a *functional summary* is in
 465 full generality any map from the space of persistence diagrams to a collection of functions,
 466 $F : \mathcal{D} \rightarrow \mathcal{F}$.

467 Upon the classical-statistical approximation, expectation values of quantum observ-
 468 ables are computed as ensemble-averages of classical field configurations, which are time-
 469 evolved via the corresponding classical equation of motion starting from fluctuating initial
 470 conditions. The range of validity of this approximation is typically restricted to high
 471 occupation numbers [31]. We propose to proceed analogously for functional summaries
 472 of persistence diagrams. To this end, any such summary F may be evaluated on the
 473 level of individual field configurations and its expectation value $\langle F \rangle$ computed as the
 474 ensemble-average. We assume that the range of validity of this approach coincides with
 475 the well-known classical-statistical regime. Certainly, for any functional summary F this
 476 proposal requires the existence of a corresponding linear operator \mathcal{F} , such that in the
 477 classical-statistical regime for any $s \in \Omega$,

$$\text{tr}(\rho(t) \mathcal{F})(s) = \langle F \rangle(t, s), \quad (11)$$

478 $\rho(t)$ being the time-dependent density operator of interest, the trace taken over the cor-
 479 responding quantum theory Hilbert space and the right-hand side being computed via
 480 the aforementioned evaluation scheme. However, the existence of such an operator \mathcal{F} is a
 481 priori not clear and will be discussed in a future work.

482 We need to assure that in the limit of averaging infinitely many individual functional
 483 summaries of field configurations the statistical mean of the functional summary is recov-
 484 ered. This is guaranteed for by a mathematical statement on the pointwise convergence
 485 of so-called equicontinuous and uniformly bounded functional summaries, the details of
 486 which can be found in Proposition 1 of Ref. [47]. For the sake of this statement we restrict
 487 our proposal to functional summaries of persistence diagrams with these two fairly general
 488 conditions. By means of the described classical-statistical evaluation scheme we refer to
 489 such functional summaries as *persistent homology observables*.

490 We want to stress that this proposal is neither restricted to the computation of persis-
 491 tent homology from equal-time alpha complexes, that is, alpha complexes computed from
 492 point clouds constructed at individual instances of time as done in this work, nor to alpha
 493 complexes themselves.

494 3.2 The asymptotic persistence pair distribution and geometric quanti- 495 ties

496 Let $F : \mathcal{D} \rightarrow \mathcal{F}$ be a functional summary in the above sense. We say that F is *additive*,
 497 if $F(D + E) = F(D) + F(E)$ for any two persistence diagrams $D, E \in \mathcal{D}$. Here, $D + E$
 498 denotes the sum of multisets, that is, the union of D and E with multiplicities of elements
 499 in both D and E added.

500 Let $D(t) \in \mathcal{D}$ be a persistence diagram computed at time t as specified in Sec. 2.3.2
 501 and F an additive functional summary. We then find for all $s \in \Omega$,

$$\begin{aligned} F(D(t))(s) &= \sum_{(r_b, r_d) \in D(t)} F(\{(r_b, r_d)\})(s) \\ &= \int_0^\infty dr'_b \int_0^\infty dr'_d F(\{(r'_b, r'_d)\})(s) \mathfrak{P}(t, r'_b, r'_d), \end{aligned} \quad (12)$$

502 with the *persistence pair distribution*

$$\mathfrak{P}(t, r'_b, r'_d) := \sum_{(r_b, r_d) \in D(t)} \delta(r'_b - r_b) \delta(r'_d - r_d), \quad (13)$$

503 δ denoting the Dirac delta function.

504 Let $(D_\ell^{(i)}(t))_{i \in \mathbb{N}} \subset \mathcal{D}$ be a classical-statistical ensemble of persistence diagrams de-
 505 scribing ℓ -dimensional persistent homology classes at time t . We denote the persistence
 506 pair distribution of $D_\ell^{(i)}(t)$ by $\mathfrak{P}_\ell^{(i)}(t)$ and define the *asymptotic persistence pair distribu-*
 507 *tion*, $\langle \mathfrak{P}_\ell \rangle$, at any time t implicitly, requiring that for any equicontinuous and uniformly
 508 bounded functional summary F as in the above proposal,

$$\begin{aligned} &\int_0^\infty dr'_b \int_0^\infty dr'_d F(\{(r'_b, r'_d)\})(s) \langle \mathfrak{P}_\ell \rangle(t, r'_b, r'_d) \\ &:= \lim_{k \rightarrow \infty} \frac{1}{k} \sum_{i=1}^k \int_0^\infty dr'_b \int_0^\infty dr'_d F(\{(r'_b, r'_d)\})(s) \mathfrak{P}_\ell^{(i)}(t, r'_b, r'_d), \end{aligned} \quad (14)$$

509 for arbitrary $s \in \Omega$.

510 Functional summaries of relevance in this work include the distribution of birth and
 511 death radii that have been defined in Eqs. (8a) and (8b), respectively. With an obstacle
 512 to be described below, both can be computed as marginal distributions of $\langle \mathfrak{P}_\ell \rangle$,

$$\langle \mathcal{B}_\ell \rangle(t, r_b) = \int_0^\infty dr_d \langle \mathfrak{P}_\ell \rangle(t, r_b, r_d), \quad (15a)$$

$$\langle \mathcal{D}_\ell \rangle(t, r_d) = \int_0^\infty dr_b \langle \mathfrak{P}_\ell \rangle(t, r_b, r_d). \quad (15b)$$

513 In addition, we define the persistence distribution, that is, the distribution of $r_d - r_b$,

$$\langle \mathcal{P}_\ell \rangle(t, r) = \int_0^\infty dr_d \langle \mathfrak{P}_\ell \rangle(t, r_d - r, r_d). \quad (16)$$

514 Natural quantities to study are the ℓ -th Betti numbers $\langle \beta_\ell \rangle(t, r)$. Intuitively, the zeroth
 515 Betti number $\langle \beta_0 \rangle(t, r)$ specifies the number of connected components minus one⁶ present
 516 in the alpha complex of radius Qr and the first Betti number $\langle \beta_1 \rangle(t, r)$ specifies the corre-
 517 sponding number of holes. Being zero in the present work, higher Betti numbers count how
 518 many nontrivial higher-dimensional homology classes are present in corresponding com-
 519 plexes. Betti numbers can be computed from the asymptotic persistence pair distribution
 520 via

$$\langle \beta_\ell \rangle(t, r) = \int_0^r dr_b \int_r^\infty dr_d \langle \mathfrak{P}_\ell \rangle(t, r_b, r_d). \quad (17)$$

521 A mathematical obstacle appears with regard to definitions such as Eqs. (15a) and
 522 (15b). A priori, the sets of functions $\langle \mathcal{B}_\ell \rangle(t, r_b)$, of $\langle \mathcal{D}_\ell \rangle(t, r_d)$, of $\langle \mathcal{P}_\ell \rangle(t, r)$ and of $\langle \beta_\ell \rangle(t, r)$

⁶We work with reduced homology groups. Thus, the zeroth Betti number actually counts the number of connected components minus one.

523 are not equicontinuous. However, only functional summaries which have this property are
 524 persistent homology observables in the sense of Sec. 3.1. For all positive σ we define

$$\zeta_\sigma(s) := \frac{1}{\sqrt{2\pi\sigma^2}} \exp\left(-\frac{s^2}{2\sigma^2}\right). \quad (18)$$

525 By convolution with it at each time individually, sets of functions such as $\langle \mathcal{B}_\ell \rangle(t, r_b)$ can
 526 be rendered equicontinuous⁷. In fact, this way Eqs. (8a) and (8b) for birth and death
 527 radii distributions arise from Eqs. (15a) and (15b). In everything that follows we omit the
 528 convolution procedure in notations. As mentioned previously, the convolution procedure is
 529 numerically irrelevant. In computations, convergence of persistent homology observables
 530 is numerically verified, cf. Appendix G.

531 The average number of persistent homology classes is encoded in $\langle \mathfrak{P}_\ell \rangle$, too,

$$\langle n_\ell \rangle(t) = \int_0^\infty dr_b \int_0^\infty dr_d \langle \mathfrak{P}_\ell \rangle(t, r_b, r_d). \quad (19)$$

532 Various length scales may be constructed from $\langle \mathfrak{P}_\ell \rangle$. An interesting length scale is the
 533 average maximum death radius $\langle r_{d,\ell,\max} \rangle(t)$, which can be computed from the asymptotic
 534 persistence pair distribution via⁸

$$\langle r_{d,\ell,\max} \rangle(t) = \lim_{p \rightarrow \infty} \left(\int_0^\infty dr_b \int_0^\infty dr_d r_d^p \langle \mathfrak{P}_\ell \rangle(t, r_b, r_d) \right)^{1/p}. \quad (20)$$

535 Analogously, the average maximum birth radius can be computed. The average number
 536 of persistent homology classes and the average maximum death (birth) radius constitute
 537 persistent homology observables as constructed above.

538 3.3 Self-similar scaling approach

539 By means of the scaling behavior visible in birth and death radii distributions, in Sec. 2.5
 540 we have already begun the study of self-similarity in persistent homology observables in
 541 the vicinity of a nonthermal fixed. Here, we introduce a more general scaling ansatz for
 542 the asymptotic persistence pair distribution. We provide a heuristic packing argument
 543 relating the appearing scaling exponents.

544 In Appendix D we provide a brief discussion on the relation between the self-similar
 545 scaling ansatz described here and known notions of self-similar scaling appearing across
 546 the literature.

547 3.3.1 Scaling ansatz to the asymptotic persistence pair distribution

548 Let $\langle \mathfrak{P}_\ell \rangle(t, r_b, r_d)$ be a time-dependent asymptotic persistence pair distribution as it ap-
 549 pears in Eq. (14). We say that $\langle \mathfrak{P}_\ell \rangle(t, r_b, r_d)$ scales self-similarly, if exponents η_1, η'_1 and
 550 η_2 exist, such that for all times t, t' ,

$$\langle \mathfrak{P}_\ell \rangle(t, r_b, r_d) = (t/t')^{-\eta_2} \langle \mathfrak{P}_\ell \rangle(t', (t/t')^{-\eta_1} r_b, (t/t')^{-\eta'_1} r_d). \quad (21)$$

⁷Indeed, for any $\sigma > 0$ a constant $C_\sigma > 0$ exists, such that for all possible functions $\langle \mathcal{B}_\ell \rangle(t, r_b)$, $\partial(\langle \mathcal{B}_\ell \rangle * \zeta_\sigma)(t, r)/\partial r = (\langle \mathcal{B}_\ell \rangle * \zeta'_\sigma)(t, r) < C_\sigma$, the prime indicating taking the first derivative. Here we employed that in the lattice framework all functions such as $\langle \mathcal{B}_\ell \rangle(t, r_b)$ are uniformly bounded.

⁸Given positive real numbers y_1, \dots, y_m , one obtains their maximum via $\max\{y_1, \dots, y_m\} = \lim_{p \rightarrow \infty} (\sum_{i=1}^m y_i^p)^{1/p}$. From this, the given formula derives.

551 Due to the time-dependence of $\langle \mathfrak{P}_\ell \rangle$ derived geometric quantities become time-dependent,
 552 too. Immediately, from Eq. (21) for birth and death radii distributions the scaling behav-
 553 ior described by Eqs. (9a) and (9b) follows. Assuming $\eta_1 = \eta'_1$, the persistence distribution
 554 scales as

$$\langle \mathcal{P}_\ell \rangle(t, r) = (t/t')^{\eta_1 - \eta_2} \langle \mathcal{P}_\ell \rangle(t', (t/t')^{-\eta_1} r). \quad (22)$$

555 The total number of persistence pairs scales as

$$\langle n_\ell \rangle(t) = (t/t')^{\eta_1 + \eta'_1 - \eta_2} \langle n_\ell \rangle(t') \quad (23)$$

556 and the average maximum death radius as

$$\langle r_{d,\ell,\max} \rangle(t) = (t/t')^{\eta_1} \langle r_{d,\ell,\max} \rangle(t'). \quad (24)$$

557 Though not explicitly given here, the average maximum birth radius scales the same way.
 558 This provides evidence for the geometric intuition of persistence length scales blowing up
 559 or shrinking in the course of time upon self-similar scaling.

560 Provided that $\eta_1 = \eta'_1$, the ℓ -th Betti numbers scale as

$$\langle \beta_\ell \rangle(t, r) = (t/t')^{2\eta_1 - \eta_2} \langle \beta_\ell \rangle(t', (t/t')^{-\eta_1} r). \quad (25)$$

561 3.3.2 A heuristic packing relation

562 We assume that $\eta_1 = \eta'_1$ and consider a general spatial dimension d here. A fairly general
 563 heuristic argument leads to the packing relation $\eta_2 = (2 + d)\eta_1$. Intuitively, the argument
 564 encodes that only a finite number of persistent homology classes of a given size can be
 565 packed into a constant volume V .

566 Let point clouds be dominated by a time-dependent length scale $L(t)$. The d -dimensional
 567 volume V in which the point clouds reside is kept constant. Heuristically, a number
 568 $\langle n_{d-1} \rangle(t)$ of $(d-1)$ -dimensional persistent homology classes fits into V , with this number
 569 scaling as

$$\langle n_{d-1} \rangle(t) \sim \frac{V}{L(t)^d}, \quad (26)$$

570 since the volume that each $(d-1)$ -dimensional persistent homology class occupies generi-
 571 cally may scale as $\sim L(t)^d$. Inferring the scaling of length scales as described by Eq. (24),
 572 that is, $L(t) \sim t^{\eta_1}$, we find

$$\langle n_{d-1} \rangle(t) \sim t^{-d\eta_1}. \quad (27)$$

573 On the other hand, from Eq. (23) we obtain

$$\langle n_{d-1} \rangle(t) \sim t^{2\eta_1 - \eta_2}. \quad (28)$$

574 Hence,

$$\eta_2 = (2 + d)\eta_1, \quad (29)$$

575 which shows that persistent homology observables represent in a direct fashion the geom-
 576 etry at hand.

577 Of course, the assignment of occupied volumes to $(d-1)$ -dimensional homology classes
 578 is highly heuristic, bearing in mind that a homology class is an equivalence class of many
 579 cycles within a simplicial complex, rendering any such mapping ambiguous. However,
 580 one may use elements of the proof of the Wasserstein stability theorem for persistence
 581 diagrams, carried out in Ref. [43], to deduce Eq. (29) more rigorously from physically
 582 reasonable assumptions. In Appendix C we sketch the corresponding derivation, provided
 583 in detail in Ref. [49].

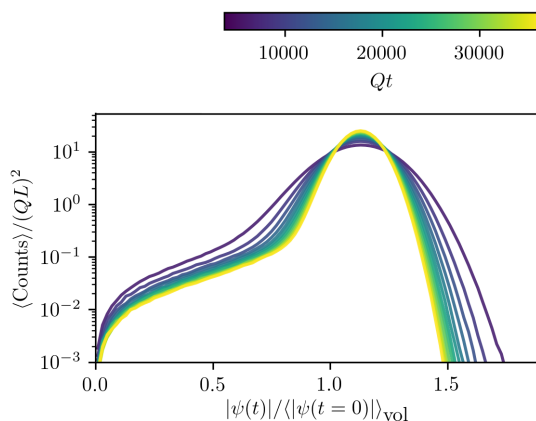


Figure 8: Distribution of amplitude-values at different times, averages taken across classical-statistical sampling runs.

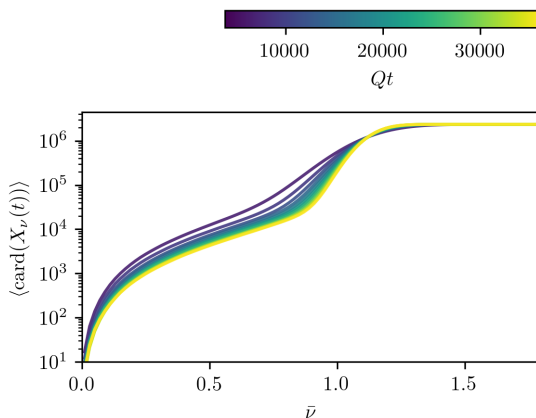


Figure 9: The average cardinality of point clouds varying with $\bar{\nu}$ at different times, averages taken across classical-statistical sampling runs.

584 4 Exponent shifts, persistences and Betti number distribu- 585 tions

586 In this section the due explanation of temporal shifts of the scaling exponent spectrum
587 observed in Sec. 2.5 is given as well as numerical outcomes for persistence distributions and
588 Betti numbers. The latter provide further evidence for the suitability of the self-similar
589 scaling ansatz for the asymptotic persistence pair distribution, as given by Eq. (21).

590 4.1 Amplitude redistribution-induced exponents shifts

591 The scaling exponents displayed in Fig. 7 change in time for $\bar{\nu} \gtrsim 0.5$. To discuss the
592 origins of this effect, in Fig. 8 amplitude distributions are displayed for different times
593 between $Qt = 3750$ and $Qt = 37500$. As is clearly visible, amplitudes redistribute with
594 growing times towards the peak at around $|\psi(t)| / \langle |\psi(t=0)| \rangle_{vol} \approx 1.05$. As indicated in
595 Fig. 9, point clouds $X_\nu(t)$ with $\bar{\nu} \lesssim 1.0$ become sparser with time, that is, for a fixed $\bar{\nu}$
596 the cardinality of point clouds decreases.

597 As deduced earlier, at low $\bar{\nu}$ -values point clouds are dominated by accumulations of

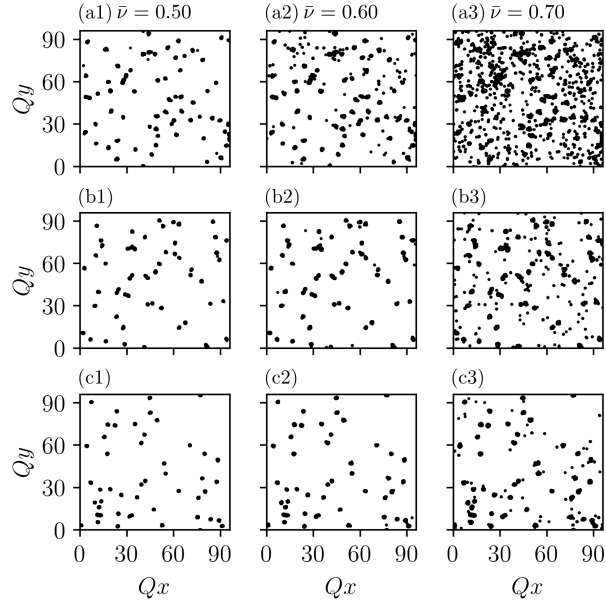


Figure 10: Example point clouds $X_\nu(t)$ for different $\bar{\nu}$ -values as indicated. Row (a): time $Qt = 3750$. Row (b): $Qt = 7500$. Row (c): $Qt = 11250$.

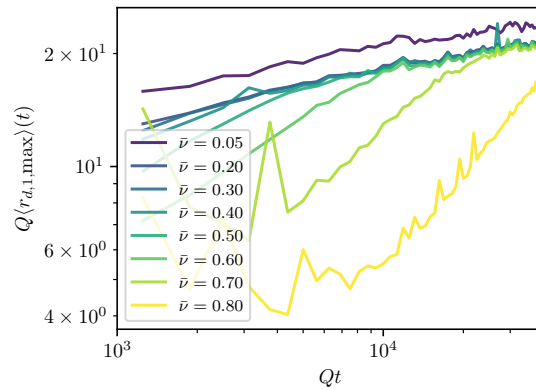


Figure 11: The average maximum death radius of 1-dimensional persistent homology classes varying with time, displayed for $\bar{\nu}$ -values as indicated.

598 points around vortex nuclei, while for $\bar{\nu} \gtrsim 0.4$ points in the bulk enter point clouds. With
 599 point clouds getting sparser in the course of time it is first bulk points to disappear from
 600 point clouds. Accumulations of points around vortex nuclei remain, as can be seen from
 601 Fig. 10, in which point clouds are displayed for different filtration parameters and times.
 602 Given the example point cloud for $\bar{\nu} = 0.5$ at time $Qt = 3750$, we observe that it is made
 603 up from accumulations of points (around vertices) mixed with random points in between,
 604 while at time $Qt = 11250$ the point cloud consists of nothing but the accumulations. The
 605 behavior of point clouds at $\bar{\nu} = 0.6$ is similar, although the point cloud at $Qt = 11250$
 606 still contains random points associated to sound excitations between accumulations. Point
 607 clouds at $\bar{\nu} = 0.70$ only get sparser but still contain many bulk points.

608 The average maximum death radius of 1-dimensional persistent homology classes,
 609 $\langle r_{d,1,\max} \rangle(t)$, is displayed for different $\bar{\nu}$ -values in Fig. 11. Comparably large fluctuations
 610 and outliers occur, since $\langle r_{d,1,\max} \rangle(t)$ is very sensitive to particular geometric arrange-
 611 ments of points in point clouds of individual classical-statistical samples. According to
 612 Eq. (24), if the system's asymptotic persistence pair distribution scales self-similarly in
 613 time and $\eta_1 = \eta'_1$, then $\langle r_{d,1,\max} \rangle(t) \sim t^{\eta_1}$. Indeed, $\langle r_{d,1,\max} \rangle(t)$ shows power-law behavior
 614 within individual periods of time and confirms the shifts in scaling exponents as indicated
 615 by the results displayed in Fig. 7, which have been deduced from birth and death radii
 616 distributions. For instance, for $\bar{\nu} = 0.6$ a shift occurs between times $Qt \approx 9000$ and
 617 $Qt \approx 13000$.

618 Recently, the phenomenon of prescaling has been discovered, that is, the rapid es-
 619 tablishment of a universal scaling form of distributions long before the universal values
 620 of corresponding scaling exponents are realized [50, 51]. Although we also study time-
 621 dependent scaling exponents of constant-form distributions, we want to stress that in our
 622 case this is not a manifestation of prescaling. Instead, it is an artifact of the sharp cutoff
 623 at the filtration parameter to generate point clouds, rendering point clouds themselves
 624 and their persistent homology groups sensitive to amplitude redistribution effects.

625 4.2 Persistence distributions

626 In Fig. 12 persistence distributions for different filtration parameters are displayed. Again,
 627 fluctuations are due to statistical uncertainties. Distributions can be rescaled using time-
 628 dependent scaling exponents as given in Fig. 7. To this end, we attribute the observed
 629 behavior to the physics at large length scales. We want to emphasize that the persistence
 630 distributions at a low filtration parameter such as $\bar{\nu} = 0.2$ show distinctly a power-law
 631 behavior at all times. A power-law fit of the rescaled distributions for $\bar{\nu} = 0.2$ reveals a
 632 scaling with persistence as $\sim (r_d - r_b)^{-\zeta}$ with⁹

$$\zeta = 1.468 \pm 0.021. \quad (30)$$

633 The relation of the exponent ζ to known signatures of for example strong wave turbulence
 634 is to date not clear to us.

635 4.3 Betti numbers as a consistency check

636 In Sec. 3.3 we derived that if the asymptotic persistence pair distribution scales self-
 637 similarly, then Betti number distributions do so as well, described by Eq. (25). Having

⁹The power-law fit is first carried out for persistence values between $Q(r_d - r_b)_{\min} = 0.3125$ and $Q(r_d - r_b)_{\max} = 5.0$ at each of the times $Qt_i = 3750, 4375, \dots, 37500$, individually, to obtain values for $\zeta(t_i)$ and its fitting error at time t_i , $\Delta\zeta(t_i)$, $i = 1, \dots, N_i$. Subsequently, the value of ζ is defined to be the average of the obtained exponents. Its error squared, $\Delta\zeta^2$, is computed by means of standard error propagation as the sum of the temporal error squared and the sum of all $\Delta\zeta(t_i)^2/N_i^2$.

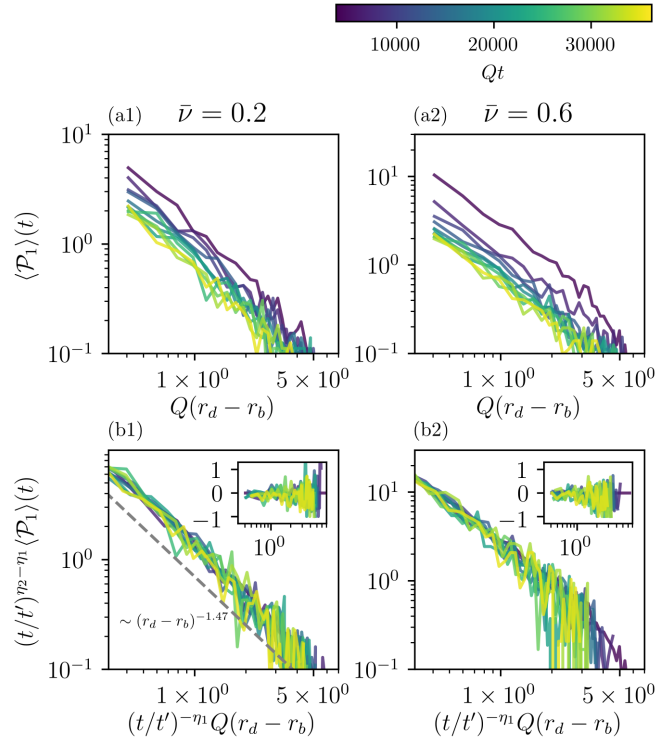


Figure 12: Persistence distributions. Each column shows data for the indicated filtration parameter, $\bar{\nu}$. The employed time-dependent scaling exponents are displayed in Fig. 7. Insets show corresponding residuals.

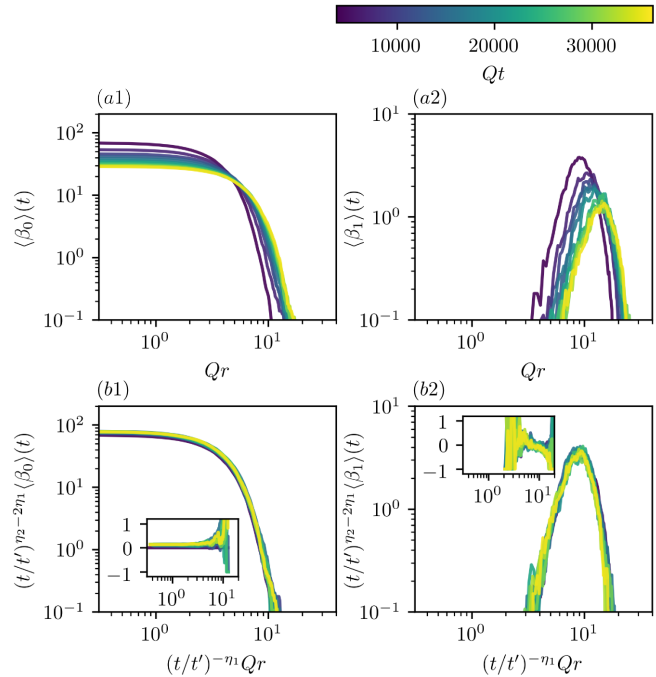


Figure 13: Betti number distributions for $\bar{\nu} = 0.2$ are shown for dimensions ℓ as indicated. The employed time-dependent scaling exponents are displayed in Fig. 7, setting $\eta'_1 := \eta_1$. Insets show corresponding residuals.

638 extracted scaling exponents from birth and death radii distributions in Sec. 2.5, we inves-
 639 tigate Betti number distributions as a consistency check.

640 In Fig. 13 Betti number distributions for both zero- and one-dimensional homology
 641 classes are displayed at $\bar{\nu} = 0.2$. For all times $\langle\beta_0\rangle(t, r)$ is a monotonically decreasing
 642 function, since zero-dimensional persistent homology classes are born at zero radius and
 643 $\langle\beta_0\rangle(t, r)$ captures only their death. We find a peak in unrescaled $\langle\beta_1\rangle(t, r)$, which, again,
 644 decreases in magnitude and shifts to higher radii as an indication of growing geometric
 645 structures.

646 Approximately, Betti numbers display self-similar scaling behavior. However, residuals
 647 of the rescaled $\langle\beta_0\rangle(t)$ increase at large radii and $\langle\beta_1\rangle(t)$ shows comparably large fluctu-
 648 ations. Nonetheless, rescaled Betti number distributions confirm previously extracted
 649 exponents.

650 5 Conclusions

651 In the present study we proposed a novel class of observables, persistent homology ob-
 652 servables, to study the dynamical behavior of quantum fields. Serving as a prototype
 653 application, we investigated the self-similar dynamics at nonthermal fixed points in the
 654 classical-statistical approximation. Accompanied by mathematical considerations that
 655 guarantee, for example, for the convergence of averages, we studied functional summaries
 656 of persistent homology groups. We found that the notion of an asymptotic persistence
 657 pair distribution is a suitable probability measure for a self-similar scaling ansatz.

658 By means of simulations of the two-dimensional nonrelativistic Bose gas we revealed
 659 that the self-similar scaling dynamics characterizing nonthermal fixed points is a phe-
 660 nomenon that also appears in persistent homology observables. Crucially, this way we
 661 discovered a continuous spectrum of scaling exponents, depending on a filtration param-
 662 eter that appears in the construction of point clouds. We provided a possible explanation
 663 in terms of scaling species mixing associated to two different dynamical processes: strong
 664 wave turbulence and anomalous vortex kinetics.

665 For all times investigated we found a power-law in persistence, possibly providing a
 666 direct indication in persistent homology observables for the presence of a turbulent cascade.
 667 It is currently unclear to us how to relate the deduced persistence power-law exponent to
 668 known power-law exponents appearing in occupation number spectra, typically signaling
 669 strong wave turbulence or hinting at topological defect structures [27, 36, 37].

670 Describing the wrapping of finite-size homology classes into a finite volume, by means of
 671 a packing relation we argued that self-similarity in persistent homology observables reflects
 672 the geometry at hand. Further exploring the relation between such geometric effects and
 673 conserved quantities associated to transport processes at nonthermal fixed points would
 674 be interesting, but lies outside the scope of this work.

675 Of particular relevance in the proposed persistent homology ansatz is the filtration
 676 function to generate point clouds from individual field configurations. We showed that
 677 already a simple variant such as the amplitude of the complex-valued fields can give
 678 rise to interesting observations. It is a feature of our analysis that the information on
 679 phase windings around vortex nuclei is not necessary in order to show the existence of
 680 further dynamical components beyond vortices. Nonetheless, we want to stress that at this
 681 point of the analysis scheme an immense freedom of choice exists, rendering the persistent
 682 homology ansatz highly flexible. Also without such a filtration procedure the proposed
 683 methods can be applied to for instance point vortex models. Surpassing the present work,
 684 one does in principle not need a lattice to construct persistent homology groups. Even

685 for fields with an arbitrary smooth and triangulable manifold as their domain there exist
686 multifarious ways to construct persistent homology groups [6].

687 Myriad of interesting further applications of persistent homology within QFT exist.
688 With regard to the recent experimental progress in handling ultracold quantum gases to
689 simulate quantum dynamics [21, 22, 30]: What can we learn from a thorough persistent
690 homology analysis of experimental data, including the investigation of different filtration
691 functions? Can relative homology groups give new geometrical insights into the relevant
692 physical processes?

693 Certainly, paths to illuminate also include analytics. Inter alia, for different types of
694 random fields statistical statements could be made [52], and by means of integral geom-
695 etry techniques predictions for alpha complexes of a class of random point clouds have
696 been derived [44]. Using similar methods, is it possible to obtain analytic predictions for
697 alpha complexes and their persistent homology in the context of quantum fields and path
698 integrals?

699 Given the present study, we believe to have found a promising machinery to understand
700 emergent connectivity and clustering structures far from equilibrium beyond the language
701 of correlation functions via geometry and topology, providing a first step on the route of
702 introducing persistent homology observables to QFT.

703 Acknowledgements

704 We thank H. Edelsbrunner, K. Ölsböck, M. Prüfer, R. Ott, L. Shen, A. Chatrchyan, T.V.
705 Zache and A.P. Orioli for discussions and collaborations on related work. We acknowledge
706 support by the Interdisciplinary Center for Scientific Computing (IWR) at Heidelberg
707 University, where part of the numerical work has been carried out.

708 **Funding information** This work is part of and supported by the DFG Collaborative
709 Research Center "SFB 1225 (ISOQUANT)", and supported by the Deutsche Forschungs-
710 gemeinschaft (DFG, German Research Foundation) under Germany's Excellence Strategy
711 EXC 2181/1 - 390900948 (the Heidelberg STRUCTURES Excellence Cluster). A.W. ac-
712 knowledges support by the Klaus Tschira Foundation, and by the National Science Foun-
713 dation under Grant No. 1440140 and the Clay Foundation, while she was in residence at
714 the Mathematical Sciences Research Institute in Berkeley, California.

715 A The mathematics of persistent homology

716 The first part of this appendix serves as an intuitive entry point to standard algebraic
717 topology concepts of relevance in this work. In the second part we construct persistent
718 homology groups more rigorously than in the main text, including structural aspects.

719 Physically speaking, in this appendix we assume that all quantities are dimensionless.
720 To this end, no factors of Q appear.

721 A.1 Relevant notions from algebraic topology

722 We introduce the notions of a simplicial complex, of chain groups and the boundary oper-
723 ator in order to finally introduce standard homology groups. For a thorough introduction
724 to algebraic topology the reader may consult, for instance, Ref. [3].

Let K be a simplicial complex. An element $\sigma \in K$ is a simplex of dimension ℓ , if $\text{card}(\sigma) = \ell + 1$. Letting $\tau \subseteq \sigma$, we call τ a face of σ , and, vice versa, σ a coface of τ . The orientation of an ℓ -simplex $\sigma = \{v_0, \dots, v_\ell\} \in K$, is an equivalence class of permutations of its vertices, $(v_0, \dots, v_\ell) \sim (v_{\pi(0)}, \dots, v_{\pi(\ell)})$ if $\text{sign}(\pi) = 1$. An oriented simplex is denoted by $[\sigma]$. Geometrically, a simplex can be realized as the convex hull of $\ell + 1$ affinely independent points in \mathbb{R}^d , $d \geq \ell$. To this end, simplices of low dimension can be thought of as vertices, edges, triangles or tetrahedra, respectively.

Subcomplexes of a simplicial complex are subsets $L \subseteq K$ that are simplicial complexes, too. A nested sequence of complexes, $\emptyset = K_0 \subseteq K_1 \subset \dots \subseteq K_k = K$ is called a filtration of the complex K .

We call the free Abelian group on the set of oriented ℓ -simplices of a simplicial complex K the ℓ -th chain group C_ℓ , where $[\sigma] = -[\tau]$ if $\sigma = \tau$ and σ and τ are oriented differently. An element $c \in C_\ell$ is an ℓ -chain, $c = \sum_i m_i [\sigma_i]$ with $\sigma_i \in K$ and $m_i \in \mathbb{Z}$. We define the boundary operator $\partial_\ell : C_\ell \rightarrow C_{\ell-1}$ to be the linear map defined by its action on a simplex $\sigma = [v_0, \dots, v_\ell] \in c$,

$$\partial_\ell \sigma = \sum_j (-1)^j [v_0, v_1, \dots, \hat{v}_j, \dots, v_\ell], \quad (31)$$

\hat{v}_j indicating that v_j is deleted from the denoted sequence. Intuitively, the boundary operator maps an ℓ -chain to its boundary, validating its nomenclature. A key feature is that $\partial_\ell \circ \partial_{\ell+1} = 0$, i.e. the boundary of a boundary is empty. Therefore the boundary operator connects the chain groups into an exact sequence, the chain complex C_* ,

$$\dots \rightarrow C_{\ell+1} \xrightarrow{\partial_{\ell+1}} C_\ell \xrightarrow{\partial_\ell} C_{\ell-1} \rightarrow \dots \quad (32)$$

To this end, the boundary group $B_\ell := \text{im} \partial_{\ell+1}$ and the cycle group $Z_\ell := \ker \partial_\ell$ are nested, $B_\ell \subseteq Z_\ell \subseteq C_\ell$.

The ℓ -th homology group is then defined as $H_\ell := Z_\ell / B_\ell$. Its elements are equivalence classes of homologous cycles. Defined over a ring \mathbb{Z} , homology groups are \mathbb{Z} -modules. However, if defined over a field such as \mathbb{Z}_2 as done in the main text, homology groups become vector spaces.

A.2 The construction and structure of persistent homology groups

We carry out the construction of persistent homology groups for the sequence of alpha complexes described in the main text, cf. Sec. 2.3.1. Let $X \subset \mathbb{R}^d$ be an arbitrary point cloud and $(\alpha_r(X))_{r \in [0, \infty)}$ its sequence of alpha complexes. The sequence is nested, $\alpha_r(X) \subseteq \alpha_s(X)$ for all $r \leq s$. X being finite, only finitely many different $\alpha_r(X)$ exist, which can be specified by means of a finite set of different r_i , $i = 1, \dots, \kappa$. We abbreviate notations by means of $\alpha_i := \alpha_{r_i}(X)$ for all i .

For all $i \leq j$, the inclusion map $\iota^{i,j} : \alpha_i \rightarrow \alpha_j$ induces a homomorphism between homology groups, $\iota_\ell^{i,j} : H_\ell(\alpha_i) \rightarrow H_\ell(\alpha_j)$, for each dimension $\ell = 0, \dots, d$. To this end, the filtration of alpha complexes yields a sequence of homology groups,

$$0 \rightarrow H_\ell(\alpha_1) \rightarrow \dots \rightarrow H_\ell(\alpha_\kappa) = H_\ell(\text{Del}(X)). \quad (33)$$

Within this sequence, homology classes are born and later die again, when they become trivial or merge with other classes. With this intuition in mind, we set

$$H_\ell^{i,j} := \text{im}(\iota_\ell^{i,j}), \quad \forall 0 \leq i \leq j \leq \kappa, \quad (34)$$

as well as

$$\beta_\ell^{i,j} = \dim(H_\ell^{i,j}), \quad (35)$$

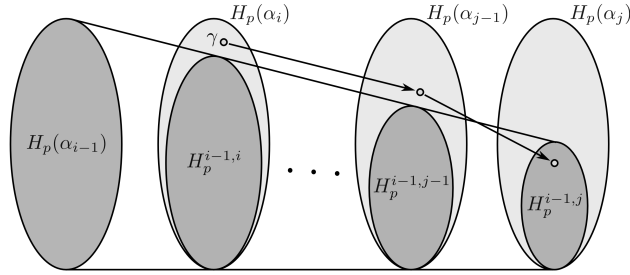


Figure 14: An illustration of the definitions of birth and death of homology classes. Picture inspired by Ref. [6].

763 counting the number of homology classes that are born at or before r_i and die after r_j .
 764 To make the notions of birth and death of a simplex rigorous, let $\gamma \in H_\ell(\alpha_i)$. We
 765 say that γ is born at α_i if $\gamma \notin H_\ell(\alpha_{i-1})$. If γ is born at α_i , then it dies entering α_j , if
 766 it merges with an older class as going from α_{j-1} to α_j , that is, $\iota_\ell^{i,j-1}(\gamma) \notin H_\ell^{i-1,j-1}$, but
 767 $\iota_\ell^{i,j}(\gamma) \in H_\ell^{i-1,j}$. The persistence of γ is defined as $\text{pers}(\gamma) := r_j - r_i$, if γ is born at α_i
 768 and dies entering α_j . For an illustration of this definition we refer to Fig. 14.

769 Actually, this intuitive definition has a conceptual drawback [2]. Any two homology
 770 classes that are born at the same birth radius r_b , one of them merging with the other
 771 one at a radius $r > r_b$, only die jointly at the death radius of the resulting homology
 772 class with highest death radius. A circumvention of this is provided by what is called
 773 the structure theorem of persistence modules [4, 5]. It states that up to isomorphism the
 774 family $((H_\ell(\alpha_i))_i, (\iota_\ell^{i,j})_{i \leq j})$ can be described by its persistence diagram as defined in the
 775 main text, cf. Sec. 2.3.2. An equivalent notion to the persistence diagram which regularly
 776 appears across topological data analysis literature is that of a barcode.

777 B The computational pipeline

778 A variety of software exists designed to provide user-friendly and fast routines for the
 779 generation of simplicial complexes and the computation of persistent homology [2]. We
 780 employ the GUDHI library, which is a generic open source C++ library tailored to topo-
 781 logical data analysis and higher dimensional geometry understanding [53]. In particular,
 782 with the simplex tree structure [54] it offers a handy data structure to store simplicial com-
 783 plexes. GUDHI employs the extensive CGAL library [55] to compute alpha complexes and
 784 uses a sophisticated algorithm to compute persistent homology groups. To give a rough
 785 indication of its speed, on a standard laptop alpha complexes of point clouds with approx-
 786 imately 100,000 data points can be analyzed in a few minutes, including the computation
 787 of persistent homology groups of all dimensions. For an overview of the computational cost
 788 of topological data analysis implementations across software solutions we refer to Ref. [2].

789 In this work we apply GUDHI functions to point clouds generated from individual field
 790 configurations according to Eq. (3). Obtaining persistent homology outcomes at various
 791 times for each field configuration, ensemble-averages are taken. Due to the lack of statis-
 792 tics, a direct analysis of the asymptotic persistence pair distribution $\langle \mathfrak{P}_\ell \rangle$ is unfeasible.
 793 Instead, for the $k = 72$ configurations investigated we have verified that the persistent
 794 homology observables $\langle \mathcal{B}_\ell \rangle(t, r_b)$, $\langle \mathcal{D}_\ell \rangle(t, r_d)$, $\langle \mathcal{P}_\ell \rangle(t, r)$ and $\langle \beta_\ell \rangle(t, r)$ converged properly.
 795 In Appendix G we analyze in detail the convergence behavior of persistent homology
 796 observables with k .

797 Of course, point clouds that are subsets of a regular lattice are generically not in general

798 position, which can result in their Delaunay complexes not being simplicial complexes.
 799 GUDHI removes corresponding ambiguities by means of a built-in perturbation scheme
 800 for points out of general position. Effects of this procedure are not visible.

801 While simulations take periodic boundary conditions into account, alpha complexes of
 802 point clouds are computed non-periodically. This comes about since a crucial function to
 803 accomplish this for two-dimensional alpha complexes is still missing in GUDHI. Certainly,
 804 the toroidal topology of the lattice Λ would have an effect on, for example, computed
 805 Betti numbers: The 2-torus has $\beta_0(T^2) = 0$, $\beta_1(T^2) = 2$ and $\beta_2(T^2) = 1$, which would at
 806 all times and radii add to $\langle \beta_\ell \rangle(t, r)$. The dynamics of point clouds and their persistent
 807 homology groups, however, would remain unaltered.

808 C Packing relation from bounded total persistence

809 In Sec. 3.3.2 we provided a heuristic argument leading to the packing relation between
 810 scaling exponents in a self-similar scaling ansatz to the asymptotic persistence pair distri-
 811 bution,

$$\eta_2 = (2 + d)\eta_1. \quad (36)$$

812 Actually, under physically reasonable assumptions this relation can be properly derived.
 813 Here we outline this deduction. Details are provided in Ref. [49].

814 In Ref. [43] the notion of bounded total persistence has been introduced for the persis-
 815 tent homology of sublevel sets of a Lipschitz function $f : M \rightarrow \mathbb{R}$ with certain properties,
 816 M being a connected, triangulable and compact metric space. For example, Lipschitz func-
 817 tions on the d -torus or the plane $[0, L]^d$, $L > 0$, have bounded total persistence. Given a
 818 point cloud $X \subset \mathbb{R}^d$ such as the $X_\nu(t)$ defined by Eq. (3), one can actually derive from
 819 the bounded total persistence an upper bound on the number of points in the persistence
 820 diagram of the sequence of alpha complexes. This upper bound scales with a particular
 821 length scale to the power of $-d$.

822 A statistical treatment of point clouds and persistence diagrams is necessary in order
 823 to define the asymptotic persistence pair distribution and the corresponding self-similar
 824 scaling ansatz. To this end, functional summaries as described in Sec. 3.1 play a key
 825 role. Properties of point clouds, persistence diagrams and functional summaries such as
 826 self-averaging in the limit of large volumes can be turned rigorous.

827 Eventually, one can obtain Eq. (36) from the upper bound on the number of points in
 828 persistence diagrams. Central to the interpretation of Eq. (36) as describing the packing
 829 of homology classes into a constant volume is this upper bound.

830 D Relating persistent homology exponents to correlation 831 function exponents

832 Typically, nonthermal fixed points and their properties are discussed in the framework of
 833 fixed-order correlation functions, both theoretically and experimentally [21, 22, 31, 56–58].
 834 The self-similar scaling behavior at nonthermal fixed points allows for a grouping of far-
 835 from-equilibrium quantum systems into universality classes. Universality classes cover
 836 broad classes of far-from-equilibrium initial conditions, large ranges of relevant parameters
 837 and even theories with very different degrees of freedom [31]. Being a natural surrounding
 838 for universality, properties of nonthermal fixed points including scaling exponents have
 839 been derived within the renormalization group [59, 60]. To this end, length scales derived

840 from scaling correlation functions are expected to blow up or to shrink with a unique
841 power-law in time.

842 If the asymptotic persistence pair distribution shows self-similar scaling as in Eq. (21),
843 then any length scale derived from it scales in time as a power-law with exponent η_1 ,
844 assuming $\eta_1 = \eta'_1$. As an example consider the average maximum death radius, defined in
845 Eq. (20) and showing scaling as in Eq. (24). In light of this geometric analogy and the
846 universality of scaling exponents at nonthermal fixed points, we expect that self-similar
847 scaling behavior as extracted from correlation functions can typically be observed also in
848 persistent homology observables.

849 E Details on the nonrelativistic Bose gas simulations

850 This appendix is devoted to provide details of the numerical setup to simulate the two-
851 dimensional single-component nonrelativistic Bose gas in the classical-statistical regime.
852 The computational implementation is undertaken similar to Ref. [31].

853 Correspondingly, in the atomic gas let a be the s-wave scattering length and n its
854 density. We define a diluteness parameter [31],

$$\zeta = \sqrt{na^3}, \quad (37)$$

855 and assume that $\zeta \ll 1$. A characteristic coherence length may be defined inversely via
856 the momentum scale

$$Q = \sqrt{16\pi an}. \quad (38)$$

857 The average density, n , can be computed from the distribution function, $f(|\mathbf{p}|)$, \mathbf{p} being
858 the momentum, via

$$n = \int \frac{d^d p}{(2\pi)^d} f(|\mathbf{p}|). \quad (39)$$

859 For the validity of the classical-statistical approximation as well as extreme nonequilibrium
860 conditions to trigger dynamics towards a nonthermal fixed point, we require a large char-
861 acteristic mode occupancy, $f(Q) \gg 1$. Then, the dynamics becomes essentially classical
862 and can be described by the time-dependent Gross-Pitaevskii equation for a nonrelativistic
863 complex bosonic field, ψ ,

$$i\partial_t \psi(t, \mathbf{x}) = \left(-\frac{\nabla^2}{2m} + g|\psi(t, \mathbf{x})|^2 \right) \psi(t, \mathbf{x}). \quad (40)$$

864 Fluctuating initial conditions, $f(\mathbf{p})$, are generated as samples of a Gaussian distribu-
865 tion with a width as described in Eq. (1). Each realization is evolved according to the
866 discretized Gross-Pitaevskii equation, numerically solving the equation on a spatial lattice
867 using a split-step method [31].

868 F 2-point correlation function results in the infrared

869 In this appendix, we study the scaling properties of a time-dependent occupation number
870 distribution $f(t, \mathbf{p})$. In this appendix, p denotes the momentum absolute value. As in
871 Ref. [31] we first define the statistical two-point correlation function

$$F(t, t', \mathbf{x} - \mathbf{x}') = \frac{1}{2} \langle \psi(t, \mathbf{x}) \psi^*(t', \mathbf{x}') + \psi(t', \mathbf{x}') \psi^*(t, \mathbf{x}) \rangle, \quad (41)$$

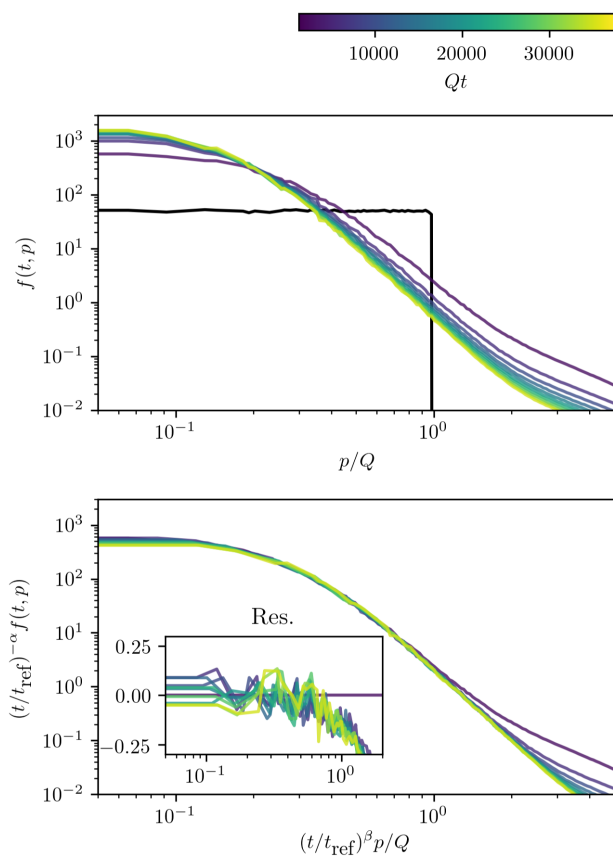


Figure 15: Occupation number distributions in the infrared. In black: The initial unrescaled occupation number distribution.

872 $\langle \cdot \rangle$ indicating evaluating the expectation value in the classical-statistical ensemble of clas-
873 sical field configurations. Subsequently, we define

$$f(t, \mathbf{p}) + (2\pi)^3 \delta^{(3)}(\mathbf{p}) |\psi_0|^2(t) \equiv \int d^3x e^{-i\mathbf{p}\mathbf{x}} F(t, t, \mathbf{x}). \quad (42)$$

874 Due to spatial isotropy of expectation values in the system, the distribution function
875 only depends on the modulus of momenta, $f(t, |\mathbf{p}|)$. The term $\sim |\psi_0|^2(t)$ represents a
876 condensate occurring in the system.

877 A scaling ansatz for the occupation number distributions, $f(t, p)$, includes two scaling
878 exponents, α and β ,

$$f(t, |\mathbf{p}|) = (t/t')^\alpha f(t', (t/t')^\beta |\mathbf{p}|). \quad (43)$$

879 In the infrared regime, a thorough numerical analysis as described in Ref. [31] yields
880 the following scaling exponents,

$$\beta = 0.189 \pm 0.011, \quad \alpha = 0.395 \pm 0.025, \quad (44)$$

881 choosing reference time $Qt' = 1250$, fitting momenta between $p/Q = 0.07$ and $p/Q = 0.7$
882 and times between $Qt = 1875$ and $Qt = 37500$. Thus, $\alpha/\beta = 2.09 \pm 0.18$. In Fig. 15
883 occupation number spectra are displayed in the infrared regime. By means of the residuals
884 the correctness of the extracted scaling exponents can be easily verified.

885 The results confirm the findings for box initial conditions in Ref. [37], in which the
886 infrared dynamics of a two-dimensional relativistic scalar field theory has been mapped to
887 that of nonrelativistic complex scalar fields. The extracted scaling exponent β is in very
888 good agreement with the prediction for the anomalous vortex kinetics nonthermal fixed
889 point in a nonrelativistic single-component Bose gas, attributed to the specific dynamics
890 of vortex defects and related vortex interactions [36]. Additionally, $\alpha/\beta \approx 2$ indicates the
891 transport of particle numbers to lower momenta [31].

892 G Numerical convergence of persistent homology observ- 893 ables

894 In this appendix we provide results for how the different persistent homology observables
895 of interest in the main text converge with the number of classical-statistical samples, k ,
896 increasing.

897 In Fig. 16 we display birth and death radii distributions as well as persistence distri-
898 butions for two values of $\bar{\nu}$, at different times within the persistent homology observables'
899 self-similar scaling regime and for different values of k . It is clearly visible that occurring
900 fluctuations decrease with k increasing.

901 In Fig. 17 we display Betti numbers. In particular $\langle \beta_0 \rangle(t, r)$ converged very well for
902 $k = 72$. $\langle \beta_1 \rangle(t, r)$ converges later with the number of samples taken into account, since
903 distributions are computed from fewer persistent homology classes with corresponding
904 properties. Yet, additional samples do not alter the overall shape of $\langle \beta_1 \rangle(t, r)$ anymore,
905 solely reducing occurring statistical fluctuations.

906 As observed in Sec. 4.1, the average maximum death radius, $\langle r_{d,1,\max} \rangle(t)$, is a quantity
907 that is very sensitive to particular geometric arrangements of points in analyzed point
908 clouds. Resembling this effect, in Fig. 18 we display $\langle r_{d,1,\max} \rangle(t)$ for different n and $\bar{\nu}$.
909 Clearly, occurring oscillations drastically reduce with k increasing. Up to a few outliers,
910 regions of approximate power-law behavior converged properly for $k = 72$ as studied in
911 the main text.

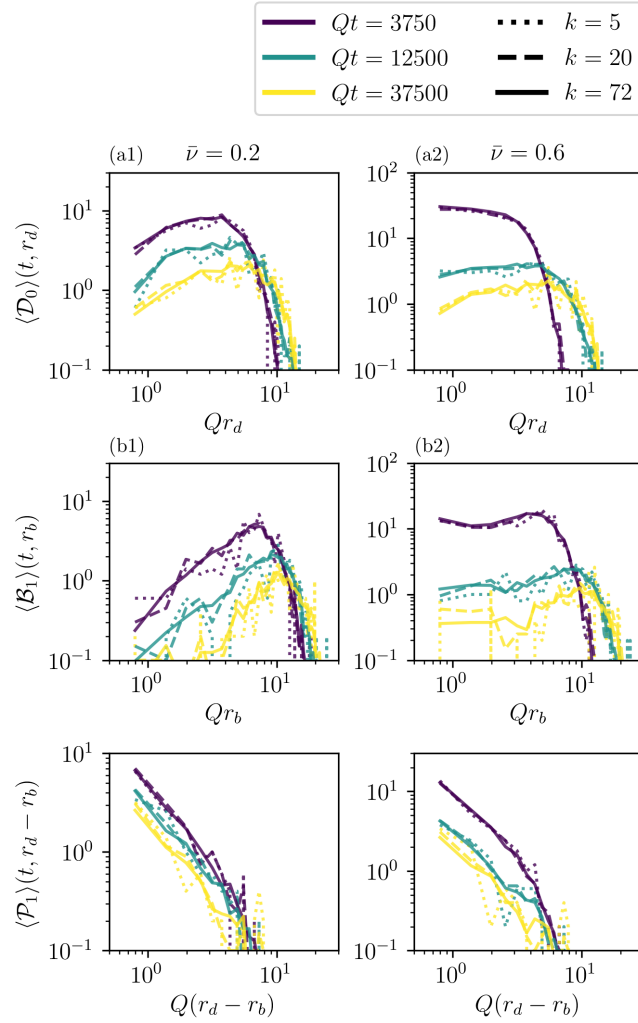


Figure 16: Birth and death radii distributions and persistence distributions in the infrared varying with time, displayed for $\bar{\nu}$ -values and numbers of samples to average, k , as indicated.

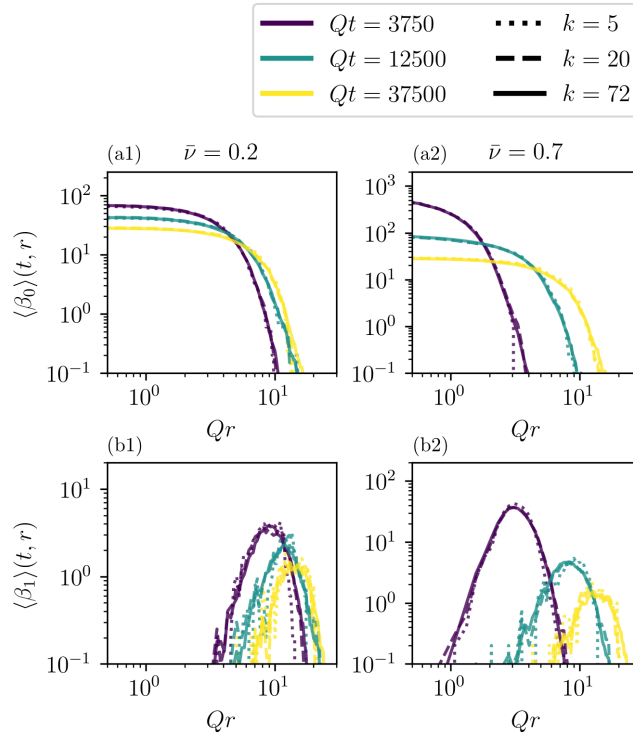


Figure 17: Betti number distributions in the infrared varying with time, displayed for $\bar{\nu}$ -values and numbers of samples to average, k , as indicated.

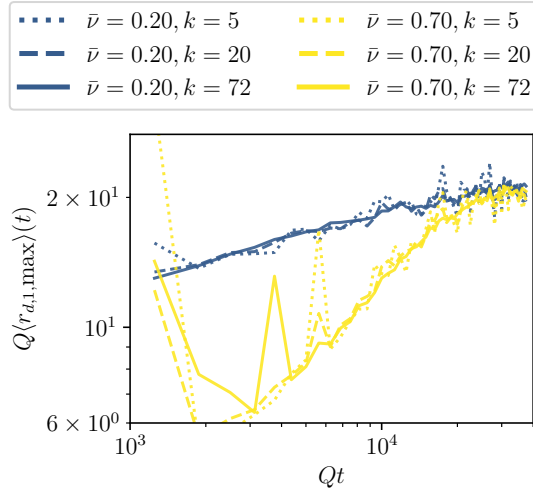


Figure 18: The average maximum death radius of 1-dimensional persistent homology classes varying with time, displayed for $\bar{\nu}$ -values and numbers of samples to average, k , as indicated.

912 To sum up, different persistent homology observables converge differently fast with the
 913 number of classical-statistical samples, k , taken into account in averaging. Corresponding
 914 differences among their convergence behavior can be easily understood geometrically.

915 H Numerical protocol to extract persistent homology scal- 916 ing exponents

917 Key to the analysis of results in our nonrelativistic Bose gas testbed in Sec. 2.5 is the
918 extraction of persistent homology scaling exponents from approximately self-similar birth
919 and death radii distributions. This appendix serves as a description of the applied protocol
920 to accomplish this task.

921 We first define rescaled variants of the birth and death radii distributions,

$$\langle \mathcal{B}_\ell \rangle^{\text{resc}}(t, r_b) = (t/t')^{\eta_2 - \eta'_1} \langle \mathcal{B}_\ell \rangle(t, (t/t')^{-\eta_1} r_b), \quad (45a)$$

$$\langle \mathcal{D}_\ell \rangle^{\text{resc}}(t, r_d) = (t/t')^{\eta_2 - \eta_1} \langle \mathcal{D}_\ell \rangle(t, (t/t')^{-\eta'_1} r_d). \quad (45b)$$

922 Distributions at later times are compared with those at the reference time t' , chosen to
923 be the time at which the self-similar evolution sets in. However, we could equally well
924 have chosen any other reference time within the self-similar scaling regime. Denote by
925 $t_k > t'$, $k = 1, \dots, N_{\text{com}}$, all corresponding comparison times. If birth and death radii
926 distributions were evolving perfectly self-similar following Eqs. (15a) and (15b), we would
927 find

$$\Delta \langle \mathcal{B}_\ell \rangle(t, r_b) = \langle \mathcal{B}_\ell \rangle^{\text{resc}}(t, r_b) - \langle \mathcal{B}_\ell \rangle(t', r_b) = 0, \quad (46a)$$

$$\Delta \langle \mathcal{D}_\ell \rangle(t, r_d) = \langle \mathcal{D}_\ell \rangle^{\text{resc}}(t, r_d) - \langle \mathcal{D}_\ell \rangle(t', r_d) = 0. \quad (46b)$$

928 Numerically, even for the correct triple of exponents $(\eta_1, \eta'_1, \eta_2)$ this is only approximately
929 true due to statistical uncertainties as well as systematic errors entering since systems
930 typically only enter the vicinity of a nonthermal fixed point. We optimize scaling exponents
931 by means of minimizing occurring deviations, quantified by

$$\chi^2(\eta_1, \eta'_1, \eta_2) = \chi_b^2(\eta_1, \eta'_1, \eta_2) + \chi_d^2(\eta_1, \eta'_1, \eta_2), \quad (47a)$$

$$\chi_b^2(\eta_1, \eta'_1, \eta_2) = \frac{1}{N_{\text{com}}} \sum_{k=1}^{N_{\text{com}}} \frac{\int_{r_{\min}}^{r_{\max}} dr_b \Delta \langle \mathcal{B}_\ell \rangle(t_k, r_b)^2}{\int_{r_{\min}}^{r_{\max}} dr_b \langle \mathcal{B}_\ell \rangle(t', r_b)^2}, \quad (47b)$$

$$\chi_d^2(\eta_1, \eta'_1, \eta_2) = \frac{1}{N_{\text{com}}} \sum_{k=1}^{N_{\text{com}}} \frac{\int_{r_{\min}}^{r_{\max}} dr_d \Delta \langle \mathcal{D}_\ell \rangle(t_k, r_d)^2}{\int_{r_{\min}}^{r_{\max}} dr_d \langle \mathcal{D}_\ell \rangle(t', r_d)^2}. \quad (47c)$$

932 Lower and upper limits of integration in the appearing expressions are set to $Qr_{\min} = 1.5$
933 and $Qr_{\max} = 25.0$ for all $\bar{\nu} \leq 0.7$ and $Qr_{\min} = 1.0$ and $Qr_{\max} = 10.0$ for $\bar{\nu} = 0.8$. A
934 priori, the given expressions for $\chi_{b/d}^2(\eta_1, \eta'_1, \eta_2)$, are equally sensitive to the behavior at
935 all scales of radii, increasing the weight of data points whose deviations are large. Linear
936 interpolations are employed to obtain birth and death radii distributions at rescaled birth
937 and death radii, respectively.

938 Minimizing deviations as measured by $\chi^2(\eta_1, \eta'_1, \eta_2)$, the optimal triple $(\tilde{\eta}_1, \tilde{\eta}'_1, \tilde{\eta}_2)$ is
939 obtained. Analogously to Refs. [31, 61], a likelihood functions is defined as

$$W(\eta_1, \eta'_1, \eta_2) = \frac{1}{\mathcal{N}} \exp \left(- \frac{\chi^2(\eta_1, \eta'_1, \eta_2)}{2\chi^2(\tilde{\eta}_1, \tilde{\eta}'_1, \tilde{\eta}_2)} \right), \quad (48)$$

940 \mathcal{N} being a normalization constant such that

$$\int d\eta_1 d\eta'_1 d\eta_2 W(\eta_1, \eta'_1, \eta_2) = 1. \quad (49)$$

941 Marginal likelihood functions are obtained upon integrating over two of the exponents, for
 942 instance,

$$W(\eta_1) = \int d\eta'_1 d\eta_2 W(\eta_1, \eta'_1, \eta_2). \quad (50)$$

943 We fit marginal likelihood functions with Gaussian distributions to estimate corresponding
 944 standard deviations, σ_{η_1} , $\sigma_{\eta'_1}$ and σ_{η_2} , the means still being given by $\tilde{\eta}_1$, $\tilde{\eta}'_1$ and $\tilde{\eta}_2$.

945 To derive time-dependent persistent homology scaling exponents, we apply the de-
 946 scribed fitting procedure with a fixed reference time Qt' for $N_{\text{com}} = 3$ times, simulta-
 947 neously: Qt_{min} as indicated in the main text as well as $Qt_{\text{min}} + 625$ and $Qt_{\text{min}} + 1250$.
 948 Repeating this procedure for different Qt_{min} , we obtain time-dependent scaling exponents.

949 References

- 950 [1] G. Carlsson, *Topology and data*, Bulletin of the American Mathematical Society
 951 **46**(2), 255 (2009), doi:10.1090/S0273-0979-09-01249-X.
- 952 [2] N. Otter, M. A. Porter, U. Tillmann, P. Grindrod and H. A. Harrington, *A roadmap
 953 for the computation of persistent homology*, EPJ Data Science **6**(1), 17 (2017),
 954 doi:10.1140/epjds/s13688-017-0109-5, 1506.08903.
- 955 [3] J. Munkres, *Elements of algebraic topology*, Advanced book program. Addison-
 956 Wesley, ISBN 9780201054873, doi:10.1201/9780429493911 (1984).
- 957 [4] Edelsbrunner, Letscher and Zomorodian, *Topological persistence and simplification*,
 958 Discrete & Computational Geometry **28**(4), 511 (2002), doi:10.1007/s00454-002-2885-
 959 2.
- 960 [5] A. Zomorodian and G. Carlsson, *Computing persistent homology*, Discrete & Com-
 961 putational Geometry **33**(2), 249 (2005), doi:10.1007/s00454-004-1146-y.
- 962 [6] H. Edelsbrunner and J. Harer, *Computational topology – an introduction*, American
 963 Mathematical Soc. (2010).
- 964 [7] H. Edelsbrunner, *Weighted alpha shapes*, Report UIUCDCS-R-92-1760. University
 965 of Illinois at Urbana-Champaign, Department of Computer Science (1992).
- 966 [8] H. Edelsbrunner and E. P. Mücke, *Three-dimensional alpha shapes*, ACM Trans-
 967 actions on Graphics (TOG) **13**(1), 43 (1994), doi:10.1145/174462.156635, math/
 968 9410208.
- 969 [9] T. Sousbie, *The persistent cosmic web and its filamentary structure – I. Theory and
 970 implementation*, Monthly Notices of the Royal Astronomical Society **414**(1), 350
 971 (2011), doi:10.1111/j.1365-2966.2011.18394.x, 1009.4015.
- 972 [10] R. van de Weygaert, G. Vegter, H. Edelsbrunner, B. J. Jones, P. Pranav, C. Park,
 973 W. A. Hellwing, B. Eldering, N. Kruithof, E. Bos *et al.*, *Alpha, Betti and the mega-
 974 parsec universe: on the topology of the cosmic web*, In *Transactions on computational
 975 science XIV*, pp. 60–101. Springer-Verlag, ISBN 9783642252488 (2011), 1306.3640.
- 976 [11] P. Pranav, H. Edelsbrunner, R. van de Weygaert, G. Vegter, M. Kerber, B. J. Jones
 977 and M. Wintraecken, *The topology of the cosmic web in terms of persistent Betti
 978 numbers*, Monthly Notices of the Royal Astronomical Society **465**(4), 4281 (2016),
 979 doi:10.1093/mnras/stw2862, 1608.04519.

- 980 [12] P. Pranav, R. J. Adler, T. Buchert, H. Edelsbrunner, B. J. Jones, A. Schwartzman,
981 H. Wagner and R. van de Weygaert, *Unexpected topology of the temperature fluctu-*
982 *ations in the cosmic microwave background*, *Astronomy & Astrophysics* **627**, A163
983 (2019), doi:10.1051/0004-6361/201834916, 1812.07678.
- 984 [13] L. Duponchel, *Exploring hyperspectral imaging data sets with topo-*
985 *logical data analysis*, *Analytica Chimica Acta* **1000**, 123 (2018),
986 doi:https://doi.org/10.1016/j.aca.2017.11.029.
- 987 [14] T. Nakamura, Y. Hiraoka, A. Hirata, E. G. Escolar and Y. Nishiura, *Persistent homol-*
988 *ogy and many-body atomic structure for medium-range order in the glass*, *Nanotech-*
989 *nology* **26**(30), 304001 (2015), doi:10.1088/0957-4484/26/30/304001, 1502.07445.
- 990 [15] R. Dridi and H. Alghassi, *Homology computation of large point clouds using quantum*
991 *annealing* (2015), 1512.09328.
- 992 [16] S. Lloyd, S. Garnerone and P. Zanardi, *Quantum algorithms for topologi-*
993 *cal and geometric analysis of data*, *Nature communications* **7**, 10138 (2016),
994 doi:10.1038/ncomms10138, 1408.3106.
- 995 [17] H.-L. Huang, X.-L. Wang, P. P. Rohde, Y.-H. Luo, Y.-W. Zhao, C. Liu, L. Li, N.-L.
996 Liu, C.-Y. Lu and J.-W. Pan, *Demonstration of topological data analysis on a quantum*
997 *processor*, *Optica* **5**(2), 193 (2018), doi:10.1364/OPTICA.5.000193, 1801.06316.
- 998 [18] J. J. Berwald, J. M. Gottlieb and E. Munch, *Computing Wasserstein distance for*
999 *persistence diagrams on a quantum computer* 1809.06433.
- 1000 [19] S. Gunn and N. Kornerup, *Review of a quantum algorithm for Betti numbers* (2019),
1001 1906.07673.
- 1002 [20] L. Polterovich, *Inferring topology of quantum phase space*, *Journal of Applied and*
1003 *Computational Topology* **2**(1), 61 (2018), doi:10.1007/s41468-018-0018-0, 1710.
1004 02983.
- 1005 [21] M. Prüfer, P. Kunkel, H. Strobel, S. Lannig, D. Linnemann, C.-M. Schmied, J. Berges,
1006 T. Gasenzer and M. K. Oberthaler, *Observation of universal dynamics in a spinor*
1007 *Bose gas far from equilibrium*, *Nature* **563**(7730), 217 (2018), doi:10.1038/s41586-
1008 018-0659-0, 1805.11881.
- 1009 [22] S. Erne, R. Bücker, T. Gasenzer, J. Berges and J. Schmiedmayer, *Universal dynamics*
1010 *in an isolated one-dimensional Bose gas far from equilibrium*, *Nature* **563**(7730), 225
1011 (2018), doi:10.1038/s41586-018-0667-0, 1805.12310.
- 1012 [23] C. Eigen, J. A. Glidden, R. Lopes, E. A. Cornell, R. P. Smith and Z. Hadzibabic,
1013 *Universal prethermal dynamics of bose gases quenched to unitarity*, *Nature* **563**(7730),
1014 221 (2018), doi:10.1038/s41586-018-0674-1, 1805.09802.
- 1015 [24] R. Micha and I. I. Tkachev, *Relativistic turbulence: a long way from preheating to*
1016 *equilibrium*, *Phys. Rev. Lett.* **90**, 121301 (2003), doi:10.1103/PhysRevLett.90.121301,
1017 hep-ph/0210202.
- 1018 [25] R. Micha and I. I. Tkachev, *Turbulent thermalization*, *Phys. Rev. D* **70**, 043538
1019 (2004), doi:10.1103/PhysRevD.70.043538, hep-ph/0403101.

- 1020 [26] J. Berges, K. Boguslavski, S. Schlichting and R. Venugopalan, *Turbulent thermaliza-*
1021 *tion process in heavy-ion collisions at ultrarelativistic energies*, Phys. Rev. **D89**(7),
1022 074011 (2014), doi:10.1103/PhysRevD.89.074011, 1303.5650.
- 1023 [27] J. Berges, K. Boguslavski, S. Schlichting and R. Venugopalan, *Universality far from*
1024 *equilibrium: from superfluid Bose gases to heavy-ion collisions*, Phys. Rev. Lett.
1025 **114**(6), 061601 (2015), doi:10.1103/PhysRevLett.114.061601, 1408.1670.
- 1026 [28] J. Berges, K. Boguslavski, S. Schlichting and R. Venugopalan, *Nonequilibrium*
1027 *fixed points in longitudinally expanding scalar theories: infrared cascade, Bose con-*
1028 *densation and a challenge for kinetic theory*, Phys. Rev. **D92**(9), 096006 (2015),
1029 doi:10.1103/PhysRevD.92.096006, 1508.03073.
- 1030 [29] T. V. Zache, T. Schweigler, S. Erne, J. Schmiedmayer and J. Berges, *Extracting*
1031 *the field theory description of a quantum many-body system from experimental data*,
1032 Physical Review X **10**(1) (2020), doi:10.1103/physrevx.10.011020.
- 1033 [30] M. Prüfer, T. V. Zache, P. Kunkel, S. Lannig, A. Bonnin, H. Strobel, J. Berges
1034 and M. K. Oberthaler, *Experimental extraction of the quantum effective action for a*
1035 *non-equilibrium many-body system* (2019), 1909.05120.
- 1036 [31] A. Pineiro Orioli, K. Boguslavski and J. Berges, *Universal self-similar dynamics of*
1037 *relativistic and nonrelativistic field theories near nonthermal fixed points*, Phys. Rev.
1038 **D92**(2), 025041 (2015), doi:10.1103/PhysRevD.92.025041, 1503.02498.
- 1039 [32] N. G. Berloff and B. V. Svistunov, *Scenario of strongly nonequilibrated Bose-Einstein*
1040 *condensation*, Phys. Rev. A **66**, 013603 (2002), doi:10.1103/PhysRevA.66.013603,
1041 cond-mat/0107209.
- 1042 [33] B. Nowak, J. Schole, D. Sexty and T. Gasenzer, *Nonthermal fixed points, vortex*
1043 *statistics, and superfluid turbulence in an ultracold Bose gas*, Phys. Rev. A **85**, 043627
1044 (2012), doi:10.1103/PhysRevA.85.043627, 1111.6127.
- 1045 [34] J. Schole, B. Nowak and T. Gasenzer, *Critical dynamics of a two-dimensional*
1046 *superfluid near a nonthermal fixed point*, Phys. Rev. A **86**, 013624 (2012),
1047 doi:10.1103/PhysRevA.86.013624, 1204.2487.
- 1048 [35] R. Walz, K. Boguslavski and J. Berges, *Large- N kinetic theory for highly occupied*
1049 *systems*, Phys. Rev. D **97**, 116011 (2018), doi:10.1103/PhysRevD.97.116011, 1710.
1050 11146.
- 1051 [36] M. Karl and T. Gasenzer, *Strongly anomalous non-thermal fixed point in a quenched*
1052 *two-dimensional Bose gas*, New J. Phys. **19**(9), 093014 (2017), doi:10.1088/1367-
1053 2630/aa7eeb, 1611.01163.
- 1054 [37] J. Deng, S. Schlichting, R. Venugopalan and Q. Wang, *Off-equilibrium infrared*
1055 *structure of self-interacting scalar fields: universal scaling, vortex-antivortex super-*
1056 *fluid dynamics and Bose-Einstein condensation*, Phys. Rev. **A97**(5), 053606 (2018),
1057 doi:10.1103/PhysRevA.97.053606, 1801.06260.
- 1058 [38] T. Simula, M. J. Davis and K. Helmersson, *Emergence of order from turbu-*
1059 *lence in an isolated planar superfluid*, Phys. Rev. Lett. **113**, 165302 (2014),
1060 doi:10.1103/PhysRevLett.113.165302, 1405.3399.

- 1061 [39] A. J. Groszek, M. J. Davis and T. P. Simula, *Decaying quantum turbulence in*
1062 *a two-dimensional Bose-Einstein condensate at finite temperature*, arXiv e-prints
1063 arXiv:1903.05528 (2019), 1903.05528.
- 1064 [40] G. Gauthier, M. T. Reeves, X. Yu, A. S. Bradley, M. A. Baker, T. A. Bell,
1065 H. Rubinsztein-Dunlop, M. J. Davis and T. W. Neely, *Giant vortex clus-*
1066 *ters in a two-dimensional quantum fluid*, *Science* **364**(6447), 1264 (2019),
1067 doi:10.1126/science.aat5718, 1801.06951.
- 1068 [41] S. P. Johnstone, A. J. Groszek, P. T. Starkey, C. J. Billington, T. P. Simula and
1069 K. Helmerson, *Evolution of large-scale flow from turbulence in a two-dimensional*
1070 *superfluid*, *Science* **364**(6447), 1267 (2019), doi:10.1126/science.aat5793, 1801.06952.
- 1071 [42] D. Cohen-Steiner, H. Edelsbrunner and J. Harer, *Stability of persistence diagrams*,
1072 *Discrete & Computational Geometry* **37**(1), 103 (2007), doi:10.1007/s00454-006-1276-
1073 5.
- 1074 [43] D. Cohen-Steiner, H. Edelsbrunner, J. Harer and Y. Mileyko, *Lipschitz functions*
1075 *have L_p -stable persistence*, *Foundations of Computational Mathematics* **10**(2), 127
1076 (2010), doi:10.1007/s10208-010-9060-6.
- 1077 [44] H. Edelsbrunner, A. Nikitenko and M. Reitzner, *Expected sizes of Poisson–Delaunay*
1078 *mosaics and their discrete Morse functions*, *Advances in Applied Probability* **49**(3),
1079 745–767 (2017), doi:10.1017/apr.2017.20, 1607.05915.
- 1080 [45] B. Delaunay, *Sur la sphere vide*, *Bulletin of the Academy of Sciences of the USSR* **7**,
1081 793 (1934).
- 1082 [46] Y. Mileyko, S. Mukherjee and J. Harer, *Probability measures on the space of per-*
1083 *sistence diagrams*, *Inverse Problems* **27**(12), 124007 (2011), doi:10.1088/0266-
1084 5611/27/12/124007.
- 1085 [47] E. Berry, Y.-C. Chen, J. Cisewski-Kehe and B. T. Fasy, *Functional summaries of*
1086 *persistence diagrams*, arXiv e-prints arXiv:1804.01618 (2018), 1804.01618.
- 1087 [48] J. Berges and D. Sexty, *Strong versus weak wave-turbulence in relativistic field theory*,
1088 *Phys. Rev.* **D83**, 085004 (2011), doi:10.1103/PhysRevD.83.085004, 1012.5944.
- 1089 [49] D. Spitz and A. Wienhard, *The self-similar evolution of stationary point processes*
1090 *via persistent homology* (2020), 2012.05751.
- 1091 [50] A. Mazeliauskas and J. Berges, *Prescaling and far-from-equilibrium hydrody-*
1092 *namics in the quark-gluon plasma*, *Phys. Rev. Lett.* **122**(12), 122301 (2019),
1093 doi:10.1103/PhysRevLett.122.122301, 1810.10554.
- 1094 [51] C.-M. Schmied, A. N. Mikheev and T. Gasenzer, *Prescaling in a far-*
1095 *from-equilibrium Bose gas*, *Phys. Rev. Lett.* **122**(17), 170404 (2019),
1096 doi:10.1103/PhysRevLett.122.170404, 1807.07514.
- 1097 [52] R. J. Adler, O. Bobrowski, M. S. Borman, E. Subag and S. Weinberger, *Persistent*
1098 *homology for random fields and complexes*, vol. Volume 6 of *Collections*, pp. 124–
1099 143, Institute of Mathematical Statistics, Beachwood, Ohio, USA, doi:10.1214/10-
1100 IMSCOLL609 (2010), 1003.1001.

- 1101 [53] C. Maria, J.-D. Boissonnat, M. Glisse and M. Yvinec, *The Gudhi library: simplicial*
1102 *complexes and persistent homology*, In *Mathematical Software – ICMS 2014*, pp.
1103 167–174. Springer Berlin Heidelberg, Berlin, Heidelberg, ISBN 978-3-662-44199-2,
1104 doi:10.1007/978-3-662-44199-2_28 (2014).
- 1105 [54] J.-D. Boissonnat and C. Maria, *The simplex tree: an efficient data structure for*
1106 *general simplicial complexes*, *Algorithmica* **70**(3), 406 (2014), doi:10.1007/s00453-
1107 014-9887-3.
- 1108 [55] A. Fabri, G.-J. Giezeman, L. Kettner, S. Schirra and S. Schönherr, *On the de-*
1109 *sign of CGAL, a computational geometry algorithms library*, *Software: Practice and*
1110 *Experience* **30**(11), 1167 (2000), doi:10.1002/1097-024X(200009)30:11<1167::AID-
1111 SPE337>3.0.CO;2-B.
- 1112 [56] J. Berges, *Nonequilibrium quantum fields: from cold atoms to cosmology* (2015),
1113 1503.02907.
- 1114 [57] A. Schachner, A. Piñeiro Orioli and J. Berges, *Universal scaling of unequal-time*
1115 *correlation functions in ultracold Bose gases far from equilibrium*, *Phys. Rev.* **A95**(5),
1116 053605 (2017), doi:10.1103/PhysRevA.95.053605, 1612.03038.
- 1117 [58] J. Berges, M. Mace and S. Schlichting, *Universal self-similar scaling of spa-*
1118 *tial Wilson loops out of equilibrium*, *Phys. Rev. Lett.* **118**(19), 192005 (2017),
1119 doi:10.1103/PhysRevLett.118.192005, 1703.00697.
- 1120 [59] A. Bray, *Theory of phase-ordering kinetics*, *Advances in Physics* **43**(3), 357 (1994),
1121 doi:10.1080/00018739400101505, cond-mat/9501089.
- 1122 [60] J. Berges and G. Hoffmeister, *Nonthermal fixed points and the functional renormal-*
1123 *ization group*, *Nucl. Phys.* **B813**, 383 (2009), doi:10.1016/j.nuclphysb.2008.12.017,
1124 0809.5208.
- 1125 [61] J. Berges, K. Boguslavski, S. Schlichting and R. Venugopalan, *Universal attrac-*
1126 *tor in a highly occupied non-abelian plasma*, *Phys. Rev. D* **89**, 114007 (2014),
1127 doi:10.1103/PhysRevD.89.114007, 1311.3005.